Surfaces and Interfaces 55 (2024) 105477

Contents lists available at ScienceDirect

Surfaces and Interfaces

journal homepage: www.sciencedirect.com/journal/surfaces-and-interfaces

Epoxy nanocomposites with dual filler system: Improving surface protection against wear and thermocyclic corrosion

Gopal krishna Bhagavatula [a,b], Snaha Leena [a,b], Kannan Murugasamy [a,b], Rasana Nanoth [a,b,*], Sabarish Narayanan [c], Alessandro Pegoretti [d], Jayanarayanan Karingamanna [a,b,*]

[a] Department of Chemical Engineering and Materials Science, Amrita School of Engineering, Coimbatore, Amrita Vishwa Vidyapeetham, India
[b] Centre of Excellence in Advanced Materials and Green Technologies (CoE-AMGT), Amrita School of Engineering, Coimbatore, Amrita Vishwa Vidyapeetham, India
[c] Department of Electronics and Communication Engineering, Amrita School of Engineering, Coimbatore, Amrita Vishwa Vidyapeetham, India
[d] Department of Industrial Engineering, University of Trento, Via Sommarive 9, 38123, Trento, Italy

ARTICLE INFO

Keywords:
Dual nanofillers
Tribology
Creep
Corrosion fatigue

ABSTRACT

This investigation explores the influence of dual nanofillers - multi-walled carbon nanotubes (MWCNT) and silicon nitride nanoparticles (SiN) - on the properties of epoxy (EP). Analyses of tribological characteristics show hybrid nanocomposite of 0.25/ 0.75 wt% of SiN/MWCNT filler system improves the wear resistance by 96 % compared to EP. Raman spectroscopy reveals a novel curing mechanism induced by SiN nanoparticles when incorporated into epoxy at room temperature, while DSC thermograms show SiN's role in enhancing the crosslinking density. Creep studies indicate that EP/SiN nanocomposites at 0.5 wt% loading reduced the creep rate by 99 % compared to EP over a 10-min duration at 60 °C. Dynamic mechanical analysis (DMA) illustrates a significant increase in storage modulus and a 13 °C increment in the glass transition temperature (T_g) for 0.5 wt% EP/SiN nanocomposites. High-resolution transmission electron microscopy (HR-TEM) ascertained the homogeneous dispersion of nanofillers in hybrid nanocomposites, suggesting improved and uniform stress transfer. SiN-based composites are more effective than MWCNT-based composites in protecting mild steel from corrosion with a coating efficiency of 87 %. The potential of SiN to reduce free amine groups responsible for the corrosion process is presented, while physisorption tests are conducted to evaluate pore size and volume in the corroded samples. Field emission scanning electron microscopy (FE-SEM) is employed to analyze worn-out and corroded surfaces comprehensively. In EMI shielding, SiN reduces reflectivity without affecting the absorptive capacity of MWCNTs, making them suitable for coatings in stealth applications.

1. Introduction

Nanofillers are gaining attention to improve the multifunctional properties of polymeric matrices, in which they are incorporated [1,2]. They exhibit strong potential in various fields, including supercapacitors [3], UV protection [4], chemical degradation [5,6] and water purification [7]. Polymers are lightweight, affordable, corrosion-resistant, and easy to produce, offering great design flexibility. They are often reinforced with nanoscale fillers to enhance their properties, creating polymer nanocomposites [2,8,9]. Even at very low wt%, these composites provide outstanding stiffness, rigidity and a high strength-to-weight ratio. Owing to their superior mechanical, thermal, and electrical qualities, they find a lot of applications in diverse sectors [10,11]. Epoxy (EP) can act as a suitable matrix for high-performance composites as it provides high stiffness, low shrinkage, excellent adhesion, heat and chemical resistance, electrical properties and ease of manufacturing [12–14]. Owing to the aforementioned properties, they are preferred for commercial and industrial uses, such as flooring, anti-corrosion coatings and automotive components [15,16]. EP, a thermosetting polymer, undergoes curing which leads to a reticulated 3D structure, the main reason behind the generally brittle nature of this material [17]. Epoxies cure differently from other resins, using a hardener instead of a catalyst. This typically involves an amine in an addition reaction, opening each epoxy ring with an active hydrogen from the

* Corresponding authors.
E-mail addresses: bhagavatulakrishna19@gmail.com (G. Bhagavatula), snahal3010@gmail.com (S. Leena), m_kannan@cb.amrita.edu (K. Murugasamy), n_rasana@cb.amrita.edu (R. Nanoth), nb_sabarish@cb.amrita.edu (S. Narayanan), alessandro.pegoretti@unitn.it (A. Pegoretti), kj_narayanan@cb.amrita.edu (J. Karingamanna).

https://doi.org/10.1016/j.surfin.2024.105477
Received 29 July 2024; Received in revised form 8 November 2024; Accepted 18 November 2024
Available online 19 November 2024

amine, following a standard stoichiometry [18]. The curing reactions of EP are accelerated at elevated temperatures [19,20], but they can also occur at room temperature [11,21,22] or a combination of both conditions [23]. The presence of residues of unreacted functional groups is the main drawback of room-temperature curing [11] whereas the size and expense of the specimen are the main constraints of high-temperature curing.

Polymer wear is the gradual material loss from a surface due to sliding or rubbing against a counterface. Tribological investigations commonly employ two sliding conditions: a) wet sliding, where a lubricant like water or oil is present during sliding, and b) dry sliding, where no lubrication is applied [24]. In dry sliding, the high crosslinking density and complex 3D structure of EP result in a high coefficient of friction and low wear resistance [25]. Unlike metals and ceramics, polymer tribology is highly influenced by the heat generated during sliding owing to friction. Therefore, using fillers that improve both tribological and thermal properties is crucial for enhancing the matrix [26]. *Namdev* et al. [27] reported that wear was lowest at 0.5wt% for EP reinforced with graphene nanoplatelets (GNP). *Hussain* et al. [28] found that EP reinforced with manganese oxide (α-MnO_2) displayed the lowest specific wear resistance at 0.5 wt% filler loading.

Recent years have seen an increase in interest for dedicated research into the viscoelastic and viscoplastic behaviour of polymers, such as stress relaxation, creep, and recovery, for a wider range of applications [29]. Due to their long chain arrangement and chain mobility, polymers typically experience creep, even at room temperature which can cause damage in the service life to the structural components [30]. Epoxy and other thermosets exhibit better creep resistance than thermoplastics crediting their crosslinked network [31]. Therefore, epoxy is reinforced with nanofillers to further enhance their creep resistance for structural and high-performance applications. When employed as reinforcement in an epoxy matrix, multi-walled carbon nanotubes (MWCNTs) significantly influence the creep behaviour. *Jian and Lau* et al. [32] revealed that when MWCNT length and weight percentage increased, the creep strain decreased. This phenomenon is attributed to the constrained movement of sliding and stretching of EP chains. *Starkova* et al. [33] found that the viscoelastic and viscoplastic behaviour of EP nanocomposites remains unaffected by the inclusion of MWCNTs (< 1 wt%). *Anand et al.* [34] incorporated pristine MWCNTs (PMWCNTs) and oxidized MWCNTs (OMWCNTs) in glass fibre/ EP composites (GE). Functionalized MWCNTs displayed better creep resistance than PMWCNTs at low temperatures (50 °C). At elevated temperatures, creep increased due to accelerated slippage of interface for PMWCNTs whereas better interaction between OMWCNTs and EP crediting their strong covalent bonds displayed superior creep resistance. *Zhang* et al. [35] compared the creep resistance of EP reinforced with fullerene (C60), MWCNTs, and single-walled carbon nanotubes (SWCNTs), respectively. MWCNTs had no discernible impact on creep behaviour, however SWCNTs and C60 showed better creep resistance. Carboxyl-functionalized MWCNTs (COOH-MWCNTs) displayed superior creep resistance than PMWCNTs when incorporated in the EP matrix crediting strong covalent interaction with the matrix [36]. *Al-Shawi* et al. [30] reinforced EP with nano silica (SiO_2) and found that the nanofiller decreased creep by ~50 % at 1 wt%. Very few studies have been conducted on EP reinforced using non-carbon-based nanofillers.

Epoxy's main applications include coatings and industrial flooring, where it must resist chemical attacks and corrosion. Thus, in such hostile conditions, EP and EP-based composites must exhibit these qualities. Corrosion, which degrades metals like mild steel (MS) into oxides, can affect polymers as well. MS is commonly used in structures but is susceptible to corrosion in offshore areas, particularly with exposure to sodium chloride (NaCl). EP's structure has free volume and pores, formed during exothermic curing, which can influence its properties. These create conduits for corrosive ions like Cl^-, SO_4^{2-}, etc. to penetrate through the coatings without much resistance [37]. Accordingly, the matrix is reinforced with nanomaterials to reduce the voids, pores and free volume for better corrosion protection [38]. *Samardžija* et al. [39] reinforced EP with spherical Aluminium (Al) nanoparticles which formed a thin protective film on the surface, preventing further oxidation and making it inert. At wt% of 0.75 nanofiller, EP/Al nanocomposite displayed superior corrosion resistance after 10 days of saltwater exposure. *Zhang* et al. [40] incorporated carboxymethyl cellulose (CMC) in EP/MWCNT composite and found that the corrosion rate sharply dropped with the incorporation of CMC nanofiller. *Khan* et al. [41] found that nano silica (F-SiO_2) enhanced the surface corrosion protection of the substrate when incorporated into the EP matrix.

Silicon nitride (SiN) is a popular structural ceramic material known for its intrinsically high strength, wear resistance, creep resistance, hardness and fracture toughness due to its strong covalent bond [42]. *Ramdani* et al. [43] incorporated SiN in polybenzoxazine and found that the filler significantly improved the stiffness by 2 GPa and T_g by 47 °C of the matrix. It was found that SiN acts as heterogeneous nucleating sites improving the crystallization characteristics when incorporated in PP [44]. When used as a filler, silicon nitride (SiN) exhibits tremendous potential as an anti-corrosion coating in the presence of corrosive electrolytes. Silane functionalized micro-SiN (S-SiN) was incorporated in the EP matrix and coated on Q235 carbon steel. The strong hydrophobic properties of S-SiN effectively slowed the diffusion of corrosive electrolytes [45]. *J.*L. *Gómez-Magallón* et al. [46] found that the inclusion of SiN improved the EP/ SiO_2 corrosion resistance to hydrogen sulfide (H_2S).

Incorporating a single nanofiller into a polymer matrix can significantly enhance certain properties but may also lead to a decline in others. To address these limitations, a dual or multi-filler system is often used to mitigate the drawbacks of the single-filler approach [47,48]. *Mahaki* et al. [49] added a dual nanofiller system of nano iron (III) oxide (Fe_2O_3) and graphene oxide (GO) to an EP matrix, achieving a 97 % reduction in mass loss and a 66 % decrease in coefficient of friction (COF) for a 0.6 wt% of Fe_2O_3@GO hybrid nanocomposite. Similarly, *Shubham* et al. [50] reported a 17.37 % increase in compressive strength and a 65.17 % improvement in wear resistance for 2 phr of TiO_2/ GnP EP hybrid nanocomposites. This study focuses on preparing a hybrid nanofiller composite that leverages the chemical inertness and mechanical properties and possibly enhances the curing of epoxy. The SiN nanofiller is known to improve the curing efficiency of EP [51] and corrosion inhibition. The 1-D MWCNTs impart a bridging effect to resist crack propagation and self-lubrication for wear resistance of the nanocomposites.

The intricate 3D crosslinked network of epoxy formed during curing can fail due to friction and wear [52]. Coatings must be wear-resistant, corrosion resistant and offer electromagnetic interference (EMI) shielding for various applications. The investigation of the synergistic effects of SiN and COOH-MWCNT dual nanofiller system in epoxy, focusing on tribology, flexural strength, viscoelastic properties, EMI shielding, thermo-cyclic corrosion resistance, and curing characteristics of the developed hybrid composite system forms the novelty of the work. Incorporating nanoparticles, especially SiN, is expected to significantly accelerate the curing process, enabling uniform and faster cross-linking due to numerous interactions at the interface. Consequently, marked improvements can be facilitated in surface-dependent properties like wear and corrosion resistance, and mechanical and viscoelastic properties. This research is also aimed to demonstrate enhancement in EMI shielding, driven by the conducting nature of MWCNTs and the insulating nature of SiN, contributing to the multifunctionality of these advanced nanocomposites. Collectively, these insights advance the design and application of epoxy materials with superior performance across various engineering domains.

2. Experimental work

2.1. Materials

The epoxy resin (LY556) and polyamine hardener (HY951) were provided by Covai Seenu and Company, Coimbatore, India. In the dual filler system, nano silicon nitride (SiN) with an average diameter of 40 nm and purity of 99 % was supplied by M/s Ultrananotech, Bengaluru, India. COOH-MWCNT was supplied by M/s Platonic Nanotech, Jharkhand, India, with an average length of 1–10 μm and an average diameter of 15 nm with a purity of 98 %.

2.2. Preparation of epoxy nanocomposites

The nanocomposites were prepared by adding the estimated quantities of nanofillers (based on weight percentages as shown in Table 1) into epoxy resin followed by mechanical mixing. A probe sonicator was used to uniformly distribute the multi-filler system into the epoxy matrix. The sonication was carried out for 30 min at ~ 25 KHz. After sonication, hardener was added in a ratio of 15 g for every 100 g of epoxy resin. The single filler and hybrid nanocomposites were left to cure at room temperature for 72 h Following ASTM guidelines, the cured nanocomposites were machined to fabricate test specimens. The stages in composite fabrication are shown in Fig. 1. The sample nomenclature is provided in Table 1. The hybrid filler content was optimized based on the mechanical properties performance in our previous work [11] and the same is followed in the present study.

2.3. Preparation of epoxy nanocomposite coatings

The epoxy nanocomposites and their hybrid nanocomposites exhibiting superior wear resistance were brush-coated on mild steel (MS) plates with dimensions 5 cm * 1 cm and an effective coating area of 4 cm * 1 cm with a uniform thickness of ~1 mm.

2.4. Characterization methods

The dry sliding wear test was performed on the epoxy and nanocomposites using pin-on-disc equipment (TR-20LE-PHM-200) at continuous 800 rpm and 50 N load. The disc had a diameter of 168 mm and a thickness of 8mm. The high carbon alloy steel used to make it was grade EN-31, which has the following composition: 0.9–1.2 wt% C, 0.1–0.35 wt% Si, 0.3–0.75 wt% Mn, and 1.0–1.6 wt% Cr. A UTE-40 make-FIE Universal testing machine (UTM) was used to carry out flexural testing following ASTM D790 standard by 3-point bending mode at a crosshead speed of 1.25 mm/min. Five samples were tested in each category. Dynamic mechanical analysis (DMA) was conducted using DMA 242 E Artemis in the temperature range of 23 °C - 150 °C at a heating rate of 5 °C/ min. Using a three-point mode, storage modulus (E') and tan delta (δ) were recorded at a constant frequency of 1 Hz. With a 514 nm excitation laser, Renishaw Metrological Systems UK's Invia Reflex Raman Microscope with Spectrometer was used for the Raman spectroscopy analysis. Each measurement was made at 50 μm, scanning from 1000 cm^{-1} to 3200 cm^{-1} during 10 s of exposure. The sample is checked at three different locations to get accurate spectra. Fourier Transform Infrared (FTIR) spectroscopy was performed using a BRUKER ALPHA II instrument in ATR mode at room temperature. The spectra were collected with a resolution of 0.4 cm^{-1} and spectrum collecting wavenumber range between 400 and 4000 cm^{-1}. Uniaxial tensile creep tests were conducted using a CREEP-1T machine at 60 °C under a constant load of 50 kg for 10 min. The dimensions of the samples were maintained as 130 mm * 10 mm * 3 mm, with a gauge length of 100mm. Differential scanning calorimetry (DSC) studies were conducted using Q20 TA instruments (USA) at a heating rate of 5 °C/ min in the temperature range of 25 °C to 200 °C in a nitrogen atmosphere. Thermal degradation was analysed using an SDT Q600 TGA at 10 °C/min, from room temperature to 700 °C. The dispersion of nanofillers in the matrix was determined using a JEOL/ JEM-2100 high-resolution transmission electron microscope (HR-TEM) with an acceleration voltage of 200 kV. The specimens were cut into thin slices using Leica FC7 ultramicrotome at −100 °C and placed on a copper grid. ZEISS GEMINI SEM 300 field emission scanning electron microscope (FE-SEM) was used to determine surface morphologies, EDAX, and colour mapping. For analysis, the specimens were sputter-coated with a thin layer of gold coating using QUORUM Q150R S. Corrosion fatigue tests were conducted using a Biologic SP-300 electrochemical workstation at a frequency range of 0.1 Hz - 10 kHz at an amplitude of ± 5mV. The tests were repeated three times for accurate results. All samples were exposed to cyclic corrosion or corrosion fatigue by keeping them immersed in a 3.5 % NaCl solution for two days at a temperature variation of 40 °C to −3 °C at 1 °C/ min and 70 % relative humidity, for 2 days. The volume intake and pore volume post degassing at 120 °C for 3 h were determined using Brunauer-Emmett-Teller (BET) analysis using Quantachrome instrument autosorb IQ-C-XR. The specimens' EMI shielding efficacy was characterized using an Anritsu vector network analyzer (VNA) 10 MHz - 20 GHz and a two-port setup using a coaxial waveguide adaptor at an X-band frequency range of ~ 8.2 GHz - 12.4 GHz.

Table 1
Sample nomenclature of epoxy and nanocomposites.

Sn No	Sample (EP/SiN/ MWCNT)	SiN nanoparticles (Wt %)	COOH- MWCNT (Wt %)	Sample code
1	EP/0/0	0	0	EP
2	EP/0.25/0.25	0.25	0.25	ESM1
3	EP/0.25/0.5	0.25	0.5	ESM2
4	EP/0.25/0.75	0.25	0.75	ESM3
5	EP/0.5/0.25	0.5	0.25	ES2M1
6	EP/0.5/0.5	0.5	0.5	ES2M2
7	EP/0.25/0	0.25	0	ES1
8	EP/0.5/0	0.5	0	ES2
9	EP/0/0.25	0	0.25	EM1
10	EP/0/0.5	0	0.5	EM2

3. Results and discussions

3.1. Tribological studies

3.1.1. Wear behaviour

Polymer wear occurs when a polymer slides against a surface, gradually eroding it. Factors like temperature, distance and surface roughness affect wear and friction. Friction is crucial in polymer tribology, softening the matrix and leading to material loss. Unlike thermoplastics, epoxy is less favoured for wear-resistant applications due to its high coefficient of friction (COF) and moderate wear resistance [53]. The specific wear rate achieved at 50 N and a sliding distance of ~4826 m with rpm of 800 for 12 min is calculated by Eq. (1) and is provided in Table 2.

$$Specific\ wear\ rate = \frac{change\ in\ weight}{sliding\ distance * load} \quad (1)$$

As seen in Table 2, EP wears out faster due to brittle fractures under shear loads. Among the samples, ES2 had the lowest specific wear rate, while EM1 displayed the lowest specific wear rate among COOH-MWCNT-based epoxy nanocomposites. ESM3 exhibited the lowest wear rate among all the hybrid nanocomposites.

Analyzing polymer tribology is complex due to the low melting point (T_m) and glass transition temperature (T_g) of polymeric materials. Friction-induced heat can soften the matrix, leading to material loss, unlike metals and ceramics that tolerate high temperatures. The curing process can create pores and free volume due to volatiles, which may cause specimen failure by reducing shear resistance during prolonged cyclic shearing and weakening covalent bonds between polymer layers

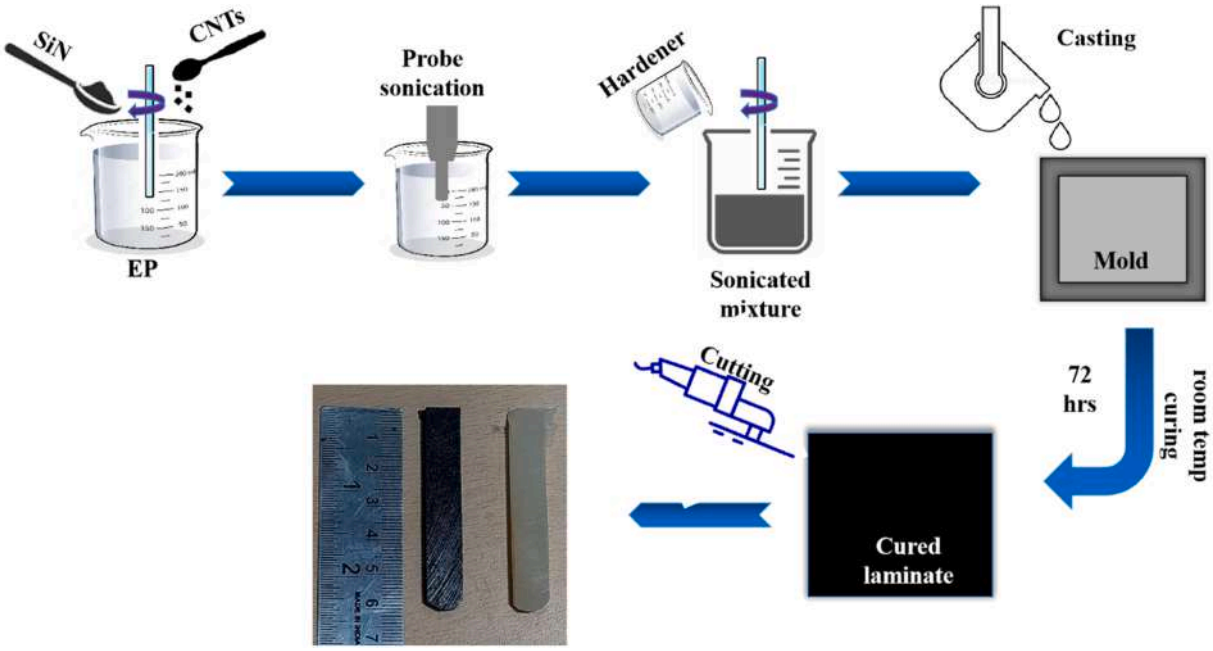

Fig. 1. Stages in the preparation of epoxy hybrid nanocomposite fabrication.

Table 2
Wear properties of epoxy, nanocomposites and hybrid nanocomposites.

Sn. No	Sample code	Specific wear rate x 10^{-8} (g/Nm)
1	EP	46.8
2	EM1	2.48
3	EM2	3.31
4	ES1	2.07
5	ES2	1.65
6	ESM1	3.31
7	ESM2	2.48
8	ESM3	2.07
9	ES2M1	3.52
10	ES2M2	2.91

[54]. Table 2 shows that the nanofillers improved the wear resistance due to their strong interaction with the matrix, which resists shearing. In contrast, EP lacks this mechanism and thus has the highest wear rate.

Ceramic nanofillers are well known to improve the wear resistance of the matrix due to their excellent load-bearing ability by reducing inter-particle distance when uniformly dispersed in the matrix [55]. SiN is known to form secondary bonds with the EP matrix as previously reported [11,51] which can lead to an increase in stiffness and increase in hardness of the nanocomposite. According to Archard's equation, wear resistance is directly proportional to hardness [56] and this theorem holds good in the present study as well. A very low wear rate was noticed for SiN-based nanocomposites when compared to COOH-MWCNT-based nanocomposites. Understanding various mechanisms behind the wear characteristics of different nanocomposites is crucial. Polymer wear, depending on the nature of polymer surface deformation (elastic, plastic, viscoelastic), results from interactions either between materials or with the counterface [57]. Material interaction can be further divided into adhesion and tribo-chemical and are heavily dependent on the polymer properties. Surface interaction can be divided into abrasion and surface fatigue.

Adhesion wear occurs when a polymer surface comes into frictional contact with the counterface. The localized bond formed between the polymer and counterface is a peculiar characteristic of this type of wear. The removed substance may remain in the crevice between the counterface's asperities or return to the polymer surface [57,58]. Removing fragments reduces asperities, resulting in a significant decrease in COF making it easier for the polymer to slide across the counterface. During the abrasion mechanism, the polymer surface is scratched by the counterface's asperities, which causes grooves or plough marks to form on the surface of the specimen. Surface fatigue occurs when the material is no longer capable of resisting the cyclic shearing whereas the tribo-chemical mechanism is a combined phenomenon of wear and corrosion where a protective layer of oxides/ burnt layers are formed. EM1 displays an adhesion mechanism crediting MWCNT's self-lubricating behaviour [58]. Table 2 illustrates the variation in mass loss of the samples with an increase in MWCNT content. Although the transfer films formed as a part of the adhesion mechanism help reduce surface roughness, they tend to continuously remove material from the surface to keep the asperities at a low level [59]. Consequently, these materials and nanocomposites are helpful in applications where new asperities are not frequently introduced and are desired to be used as rotating components.

3.1.2. Coefficient of friction (COF)

The coefficient of friction (COF) is the ratio of the tangential force (frictional) to the normal force. Since polymers in general are thermal insulators, friction is an important factor as it produces heat during sliding. The material may fail as a result of the matrix softening due to heat accumulation. Increased compressive forces from higher loads and rpm, when coupled with friction, can significantly raise the temperature of the specimen-counterface contact. Fig. 2 shows the variations in COF of EP, ES2, EM1 and ESM3, respectively. EM1 displayed the lowest COF (~0.61) in steady state when compared to EP (~0.83). Carbon nanofillers are well known to display self-lubrication [11,60] when incorporated in the polymer matrix along with transfer film formation which reduces COF drastically. ESM3 hybrid nanocomposite displayed high COF but low wear rate indicating controlled wear and prevention of the exposure of inner polymer layers to the counterface. EP displayed marching COF due to the failure of its surface resulting in an exponential rise in wear rate.

3.1.3. Wear surface analysis

Fig. 4 shows the worn-out surfaces of EP, ES2, EM1 and ESM3, respectively. Transfer films and grooves are the result of material

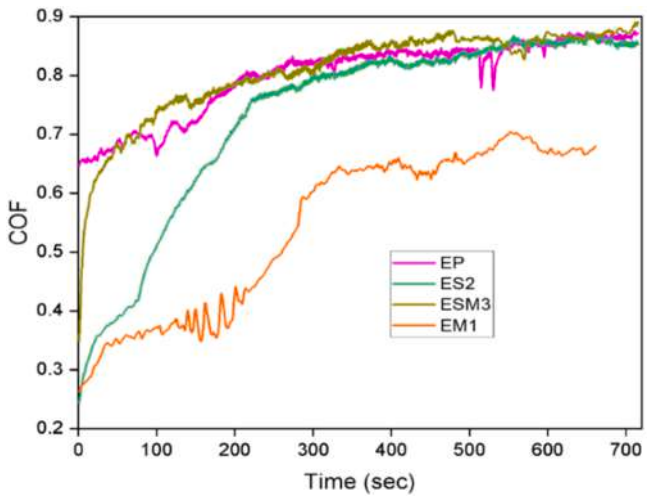

Fig. 2. Coefficient of friction (COF) of EP, ES2, EM1 and ESM3 with time.

interactions and tension generated by thermal breakdown [61]. EP experienced severe fatigue, which resulted in surface failure, fracture formation and appreciable wear. This can be explained by the polymer's limitation to tolerate large shear forces and ineffective stress transfer throughout the brittle matrix. With a high COF and abrasive ploughing mechanism, ES2 demonstrated stability and minimal mass loss. Since transfer films are not produced by the abrasion mechanism, their presence is not observed, except for a small amount of debris. The ceramic nature of SiN and its capacity to promote secondary bond formation and curing [11], offer resistance to shearing and thermal degradation, which are responsible for the reduction in wear. EM1 generated transfer films due to adhesion mechanism as seen in Fig. 3, which led to a sharp reduction in the overall COF. The synergism of dual fillers in ESM3 hybrid nanocomposite demonstrated both adhesion and abrasion mechanisms by generating tire marks and transfer films. The overall wear resistance of the specimen is enhanced by MWCNT's self-lubricating properties and SiN's resistance to shear stresses.

The composites which demonstrated outstanding wear resistance in individual and hybrid nanofiller systems were selected for further analysis using different characterization techniques. Accordingly, advance studies were carried out on EP, ES2, EM1 and ESM3 nanocomposites.

3.2. Curing behaviour

Thermosetting polymers achieve topological stability and enhanced mechanical and thermal properties through curing. Epoxy resin, a low molecular weight oligomer with one or two highly reactive epoxide groups, undergoes this process. Curing, which involves a chemical reaction with a hardener, can occur at room temperature or elevated temperature. In this work, DGEBA (two epoxide groups per molecule) reacts with aliphatic amine (TETA) at room temperature. It is well known that in comparison to room-temperature cured systems, high-temperature cured systems exhibit increased glass transition temperature (T_g), strength, and stiffness. The gel point is reached when the crosslinks branch out throughout the system and the resin no longer dissolves in the parent resin's solvent [62]. The degree of crosslinking can be significantly increased through diffusion-controlled curing, resulting in a system with a modulus of vitrified or glassy material. Secondary curing, or vitrification, occurs when the temperature of

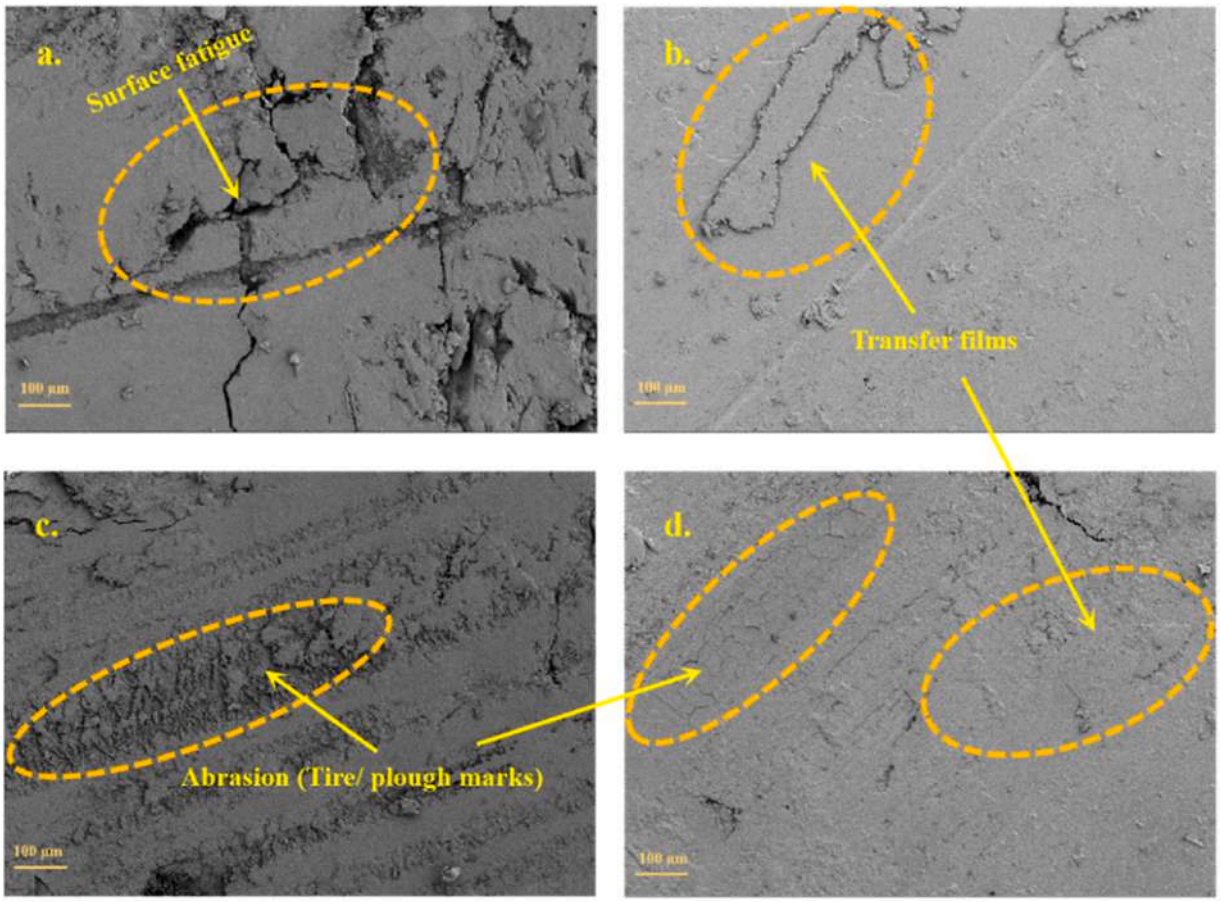

Fig. 3. FESEM images for worn-out surfaces of a. EP, b. EM1, c. ES2 and d. ESM3.

networks formed reaches the cure temperature. The major drawback of room temperature curing is the steric hindrances and remnants of functional groups which lead to partial or improper curing and result in an imperfect 3-D crosslinked structure [11].

3.2.1. Raman and FTIR spectroscopic analyses

As a part of the curing process, the 3D network of polymer chains formed alters the matrix's structure and chemical characteristics. In this section, the effect of single and hybrid nanofillers on the chemical structure of epoxy nanocomposites are investigated by means of Fourier transform infrared spectroscopy (FTIR) and Raman spectroscopy.

Fig. 4 depicts the Raman spectra of EP, ES2, EM1 and ESM3, respectively. The inclusion of SiN in epoxy has significantly improved the degree of curing of the epoxy matrix. The peak formed at ~1250 cm^{-1} indicates the consumption of free epoxide groups during vitrification and can be attributed to the ring opening and the formation of complex network structures of epoxy chains [63]. This process is much improved by SiN, and the higher thermal conductivity of the nanofiller may be responsible for this phenomenon. Since curing is an exothermic process, and epoxy being a poor conductor of heat, there may be possibilities for the presence of uncured regions in the polymer due to improper heat distribution in the system. By significantly reducing local heat spots [64] and accelerating curing, this ceramic nanofiller can further promote ring opening at room temperature along with uniform distribution of the heat generated. The ring opening mechanism of epoxy chains is not affected by COOH-MWCNTs, as evidenced by Fig. 4 for EM1 and EP. However, the hybrid nanocomposite ESM3 showed a modest increase in intensity because of the presence of SiN.

The peak at ~1600 cm^{-1} indicates an increase in curing degree [65]. In fact, SiN accelerates the curing reaction by promoting the ring opening mechanism at room temperature, which generates active sites for crosslinking to occur thereby increasing the intensity for ES2. In EM1, this effect is not discernible, and in ESM3, there is a minor increase in intensity due to the presence of SiN. The peak in the range of ~2400 - 2500 cm^{-1} indicates O—H symmetric stretching. The splitting of the hydrogen (O—H - N-Si) peak indicates strong bonds which can be observed in the case of ES2 and a broad single peak for EP is suggestive of weak or moderate hydrogen bonds [66]. Small peaks with low intensity in EM1 and ESM3 show the symmetric vibration of O—H in the COOH functional group present on the surface of MWCNTs. The intensity increase at ~2800 cm^{-1} for EM1 and ESM3 is due to the G` band of MWCNTs (~2700 cm^{-1}) [67] and the rise in ES2 intensity can be credited to CH_2 stretching, as SiN promotes ring opening of epoxy groups. The sharp increase in intensity at ~2900 cm^{-1} for ES2 and ESM3 can be attributed to the reduction in epoxy groups due to the ring-opening mechanism leading to the formation of CH_2 bonds. The idea that SiN serves as a key agent for the ring opening mechanism at room temperature is further supported by the invariance of the EM1 and EP peaks at ~2900 cm^{-1}. The amine, amide and O—H overlapping peaks can be noticed at ~3150 cm^{-1}. The O—H groups present in COOH-MWCNT increase the intensity for EM1 and N–H hydrogen bonds formed by SiN with the O—H group in the DGEBA chain increasing the intensity for ES2. The hardener remnants in EP display N—H peaks in the spectra. From the following spectroscopic analysis, it can be commented that SiN plays a crucial role in the increase in the curing degree of epoxies at room temperature.

Fig. 5 presents the FTIR spectra of EP, ES2, EM1 and ESM3, showcasing the filler-matrix interactions. Peaks at approximately 824 cm^{-1} and 1243 cm^{-1} correspond to epoxy functional groups [22]. The peaks in the range of 2190 cm^{-1} indicate symmetrical and asymmetrical stretching of the C—H group. For the EP spectrum, the stretching observed around 3390 cm^{-1} suggests the presence of excessive -OH and -NH groups in the system. The absence of these peaks in the spectra of ES2 and ESM3 implies the formation of secondary bonds between SiN and the -OH groups in the resin [11]. This absence may also suggest a ring-opening mechanism facilitated by SiN, further reinforcing the similar observations from Raman spectroscopy. Additionally, a small peak around 3390 cm^{-1} corresponds to the oscillation of the carboxyl groups in the -COOH functionalized MWCNTs [51].

3.2.2. Ring opening mechanism

Curing is an exothermic reaction and can directly influence the properties displayed by the final product. In room-temperature curing, the heat generated is not distributed uniformly, which might result in residual functional group remnants in the matrix. As already established by Raman spectroscopy, SiN is essential for triggering the system's effective ring opening of epoxy groups at ambient temperature. A scheme (Fig. 6) is proposed to further explicate this novel mechanism.

The ring opening efficiency observed in Raman spectra can be attributed to the augmentation of crosslinked bonds generated by the presence of SiN. This can be credited to SiN's excellent thermal storage capabilities. The superlative thermal storage nature of SiN was previously reported in phase-changing materials (PCMs) [69,70]. During curing, the heat liberated in the matrix is retained by SiN, which can be visualized as a hot ball of energy. The energy released from the hot ball source assists in curing processes between epoxy resin and hardener.

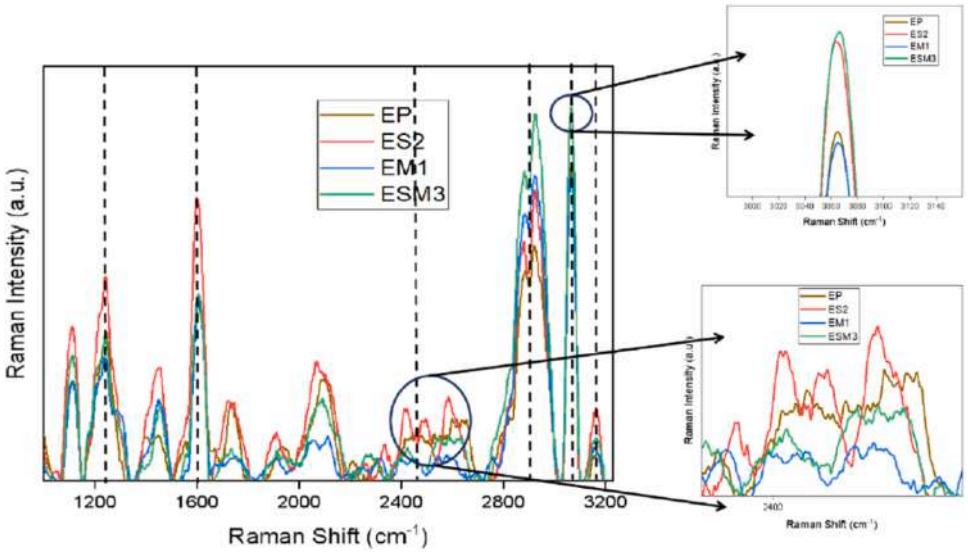

Fig. 4. Raman spectra of EP, ES2, EM1 and ESM3.

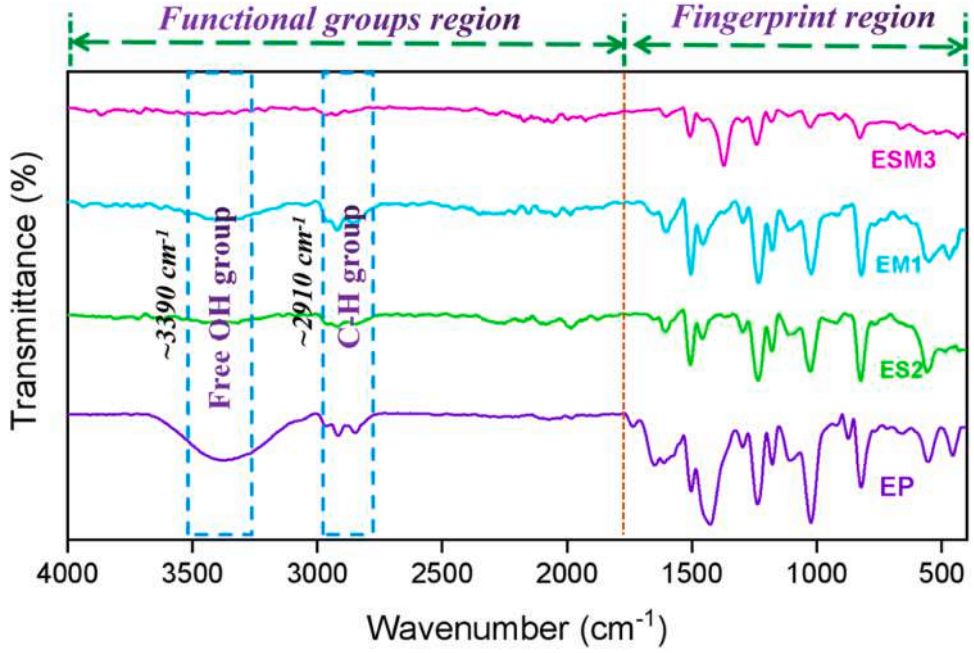

Fig. 5. FTIR spectra of cured EP, ES2, EM1 and ESM3.

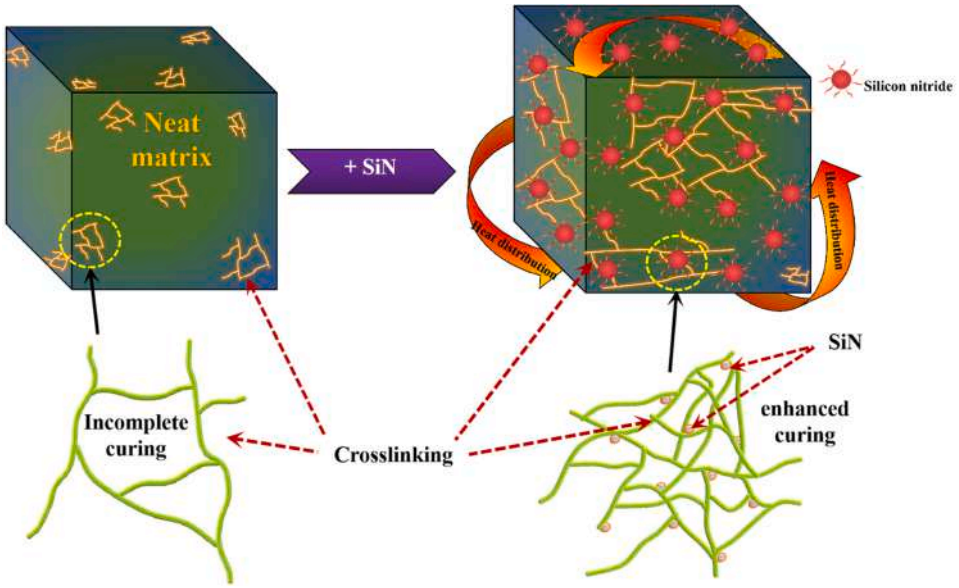

Fig. 6. Influence of SiN on curing of epoxy resin.

Furthermore, the ring opening of epoxy chains is also facilitated by the heat released which increases the curing degree as seen in Fig. 6. This novel mechanism helps in reducing remnants of functional groups, encourages near-to-complete curing of epoxy, reduces defective sites and provides improvement in final properties.

3.2.3. Differential scanning calorimetry (DSC) and thermogravimetric analysis (TGA)

A powerful method to investigate the curing characteristics of thermosetting polymers, particularly epoxy, is differential scanning calorimetry (DSC). The curing of epoxy is largely dependent on the number of epoxide groups per molecule, the stoichiometric ratio of hardener with epoxy and the heating conditions (elevated and room temperature). From previous discussions, it is clear that SiN significantly enhanced the EP matrix's crosslinking capabilities. Accordingly, the focus of analysis in this section is the shift in curing degree in EP and ES2. The heating thermogram of room temperature cured epoxy systems exhibits vitrification, or secondary curing, as a result of steric hindrances and functional group residues [68]. The exothermic peak in the thermogram, as noticed in Fig. 7, is a manifestation of secondary curing of the EP and ES2.

Since the curing reaction is exothermic, it can be assessed by the amount of heat flow in the heating cycle as epoxy is a thermoset and requires no cooling cycle to observe recrystallization. The degree of cure, which is the total heat emitted at a given time in the curing history relative to the total heat of reaction, is crucial in understanding the curing efficiency. The degree of cure or curing degree (α) can be found from Eq. (2) [71]:

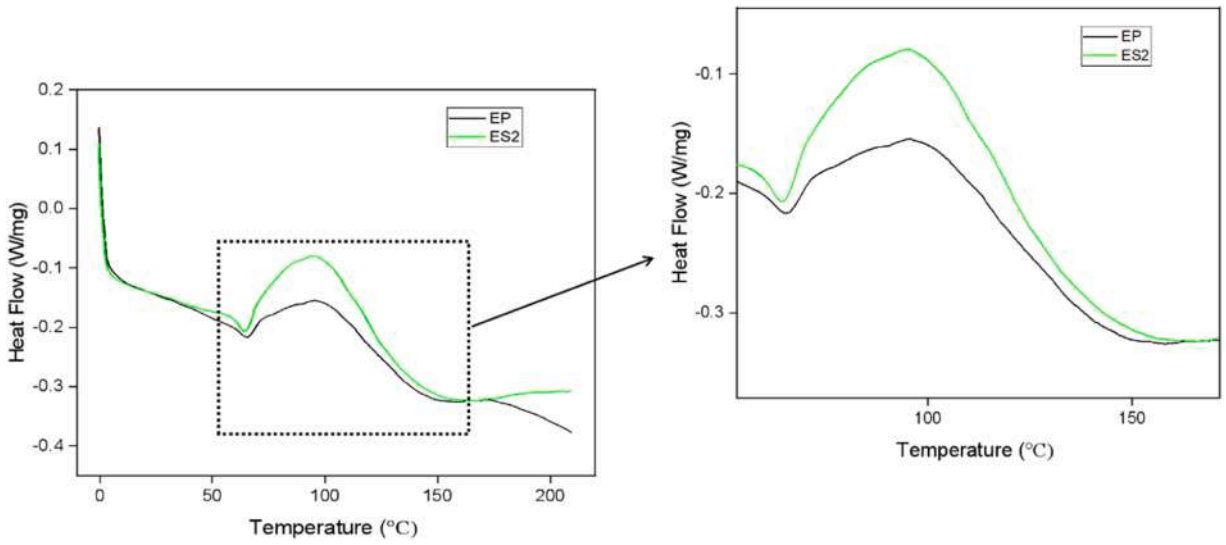

Fig. 7. DSC heating thermograms of EP and ES2.

$$\alpha(t) = \frac{\Delta H_{Res}(t)}{\Delta H_{total}} \quad (2)$$

Where, $\Delta H_{Res}(t)$ is the residual heat released at a particular time during vitrification curve history and ΔH_{total} is the total heat released during secondary curing. The curing degree for EP and ES2 is found from **Eq. [2]** w.r.t. temperature and time, respectively. From Fig. 8 **and** Fig. 9**,** it can be noticed that ES2 cured completely at lower temperatures and required less time when compared to EP. The temperature at which the curing degree achieves 10 % (α_{10}) w.r.t. temperature for ES2 and EP are 74.2 °C and 76.1 °C, respectively. The curing degree at 60 % (α_{60}) w.r.t. temperature for ES2 and EP are 126.2 °C and 127.8 °C, respectively. Complete curing, i.e., curing degree at 100 % (α_{100}) w.r.t. temperature for ES2 and EP occurred at 145.5 °C and 153.1 °C, respectively.

The duration taken for ES2 to reach α_{10}, α_{60} and α_{100} were 1.67 min, 12.21 min and 16.11 min, respectively whereas for EP to reach α_{10}, α_{60} and α_{100} were 2.05 min, 12.61 min and 17.72 min, respectively. When compared to EP, the ES2-based nanocomposites require less time to cure completely, which may be attributed to the fact that there are fewer remnant functional groups because of the unique curing mechanism that SiN exhibits as elucidated in Section 3.2.2**.** The sharp exothermic peak for ES2 in Fig. 7 can be assigned to the increase in curing degree.

A wavy curve can be noticed for ES2-based nanocomposites in Fig. 8 **and** Fig. 9. This may be due to the excellent thermal storage capacity of SiN. The heat accumulated in SiN during the heating cycle is first released between α_{10} to $\alpha_{30,}$ which triggers early vitrification and shows a steeper curve in comparison to EP. The system reaches a recharging state when a dip is observed between α_{30} and α_{50}, showing the heat is being stored by SiN along with secondary curing occurring due to heat provided during the thermal characterization. From α_{50} to α_{100}, the heat stored by the nanofiller is sharply released along with an increase in heat flow during the heating cycle, accelerating the curing reaction.

The various parameters obtained from thermal degradation studies, of EP and its nanocomposites, carried out at a heating rate of 10 °C/min are tabulated in **Table S1**. T_{100} is the temperature at which the onset of degradation occurs, and T_{50} is the temperature at which 50 % of the sample weight is lost. T_{max} represents the temperature at which the degradation rate is maximum, as obtained from the DTG curve **(Figure S1).** From **Figure S2,** it is observed that the presence of inter-connected mesh-like structures formed by long-wavy CNTs delayed the matrix degradation in EM1 [72]. This can be further evidenced by a 13.6 % reduction in the weight loss rate of these samples when compared to neat EP. ES2 exhibited an increase of 13 °C for T_{100} compared to EP, displaying a characteristic right-shift of the shoulder of the

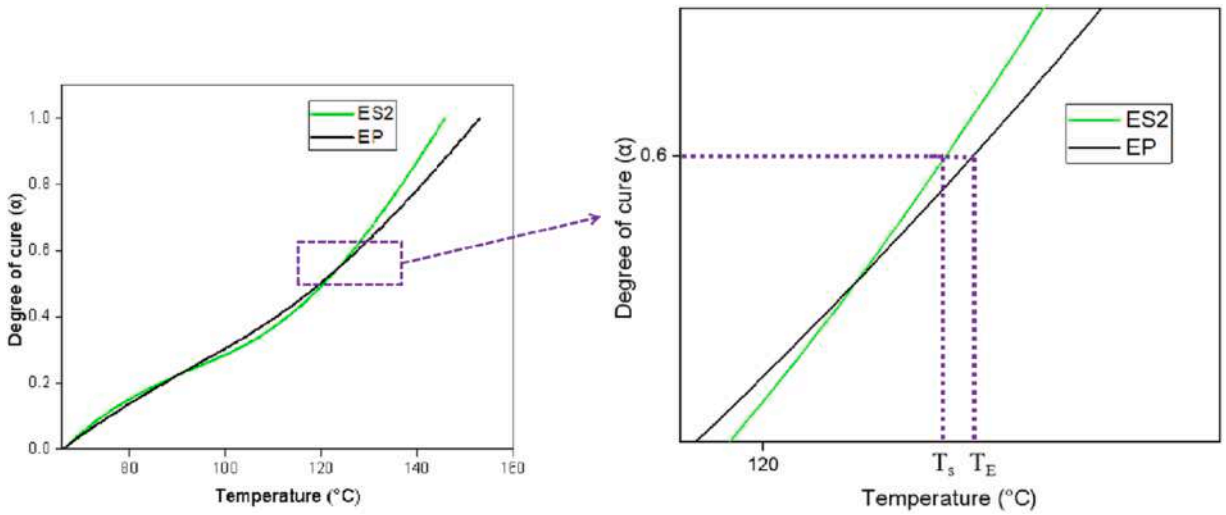

Fig. 8. Variation of curing degree with Temperature for ES2 and EP; T_s and T_E are the temperatures of ES2 and EP, respectively.

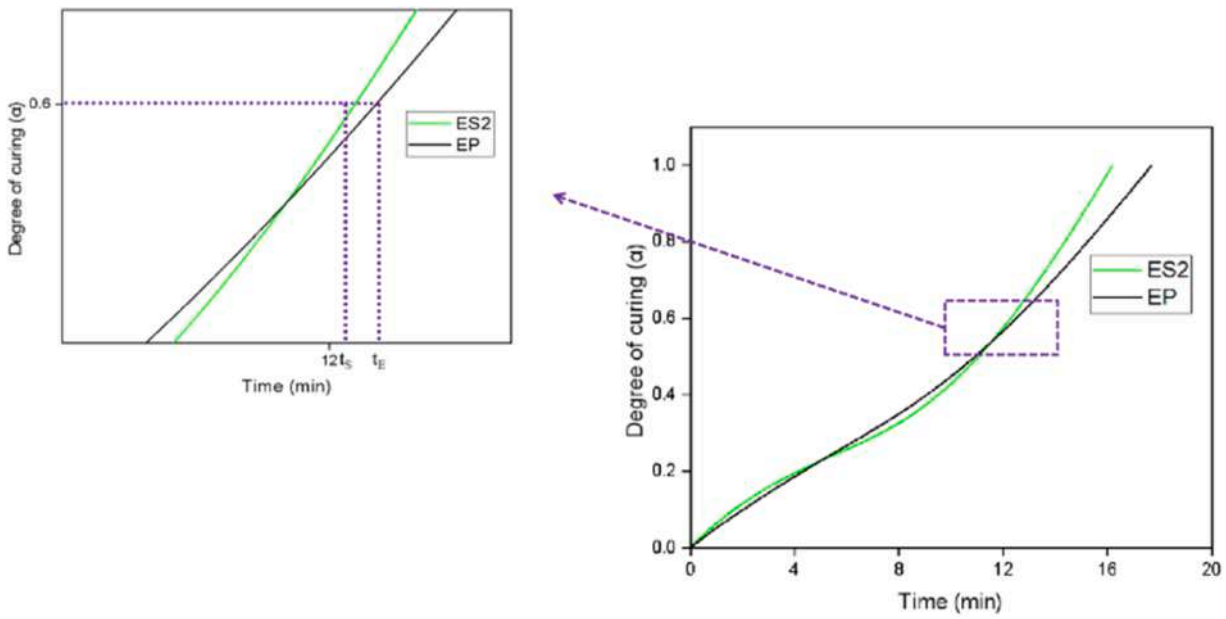

Fig. 9. Variation of curing degree with Time for ES2 and EP; (t_s and t_E being time for ES2 and EP, respectively).

thermograms. The incorporation of SiN increases thermal conductivity which improves crosslinking density, making it cumbersome to break the bonds of the polymer chains even at elevated temperatures [73]. The same feature was manifested in ESM3, due to the synergistic effect of CNT and SiN, exhibiting 5.4 % and 4.2 % increments in $T_{100\ \%}$, and T_{max}, respectively with regard to EP.

Based on Raman spectra, FTIR, curing degrees at various locations obtained from DSC curves, TGA thermograms and the scheme presented in Fig. 6, SiN is crucial for raising the matrix's crosslinking density at room temperature. By using this ceramic nanofiller, the composites fabricated at room temperature can achieve crosslink densities closer to those prepared at higher temperatures, thereby drastically reducing the processing time and thermal energy expense.

3.3. High resolution - Transmission electron microscopy (HR-TEM)

The most efficient way to assess the morphology and dispersion of nanofillers in the matrix is using TEM [21]. The synergistic interaction between the two nanofillers could be evidenced from Fig. 10**b**. The breakage and attrition of MWCNTs were not noticed in the images indicating a high aspect ratio and capability for effective stress transfer. This also enables the unique bridging mechanism displayed by this 1-D nanofiller which drastically improved fracture toughness as reported in our previous work [11]. Uniform dispersion of nanofillers in the matrix can be seen in Fig. 10**a** which reduces local stress concentration points, thereby improving overall properties.

3.4. Flexural properties

The flexural strength and modulus of the samples are presented in Fig. 11**b.** EP displayed the lowest bending strength and modulus of 106.6 ± 1.2 MPa and 2.4 ± 0.3 GPa respectively, whereas ES2 displayed the highest strength and modulus of 320 ± 1.3 MPa and 3.1 ± 0.1 GPa. This can be attributed to the superior rigidity of the samples attained by the peculiar curing behaviour of SiN and the formation of secondary bonds [11] with the matrix, improving the composite's load-bearing properties. The inclusion of MWCNTs increased the strength and modulus to 133.3 ± 1.5 MPa and 2.7 ± 0.2 GPa respectively. This increase can be credited to the bridging effect of CNTs [22,74] which hindered the crack advancement. ESM3 showed a strength of 213 ± 1.5

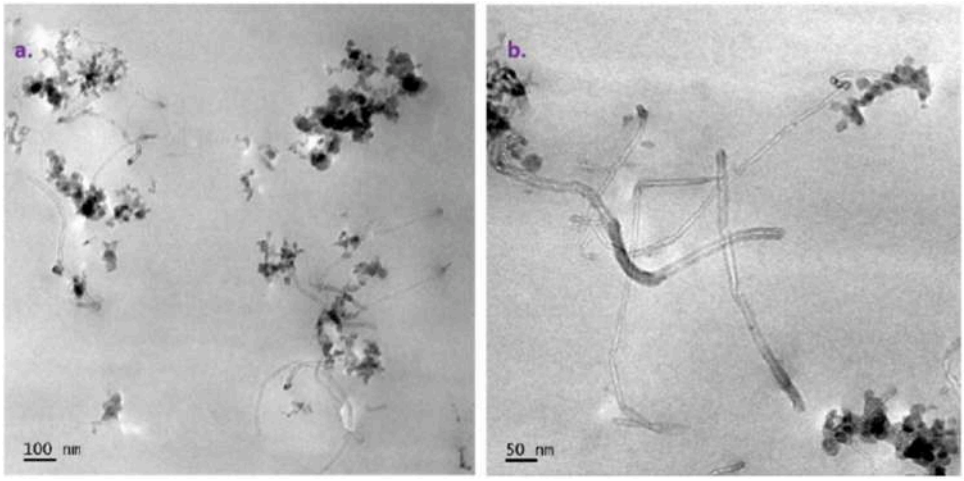

Fig. 10. HR-TEM images of SiN and COOH-MWCNT a. dispersed in EP matrix and b. their interaction.

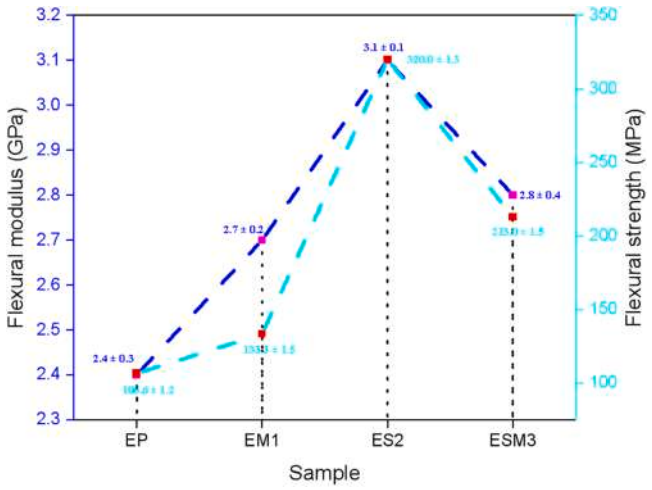

Fig. 11. Flexural properties of EP, EM1, ES2 and ESM3.

MPa and a modulus of 2.8 ± 0.4 GPa credited to the increase in crosslinks by SiN and the bridging effect of CNTs.

3.5. Dynamic mechanical analysis (DMA)

Dynamic mechanical analysis (DMA) is an approach that is frequently employed for determining the viscoelastic behaviour of polymers and their composites concerning their primary relaxations and other features like crosslinking density, T_g, stress-relaxation modulus, interfacial contact, etc. [75]. It is known that thermosetting polymers, like epoxy, undergo curing and thereby generate crosslinked bonds. The two unique processes that take place while epoxy resin cures are vitrification and gelation [21]. The resin changes phases during the gelation stage, going from a liquid to a solid rubbery state. The phenomenon known as vitrification occurs when the resin transforms from a rubbery to a glassy state as a result of an increase in molecular weight and a decrease in molecular mobility. Vitrification raises the resin's glassy quality and moves the curing temperature towards the glass transition temperature. All curing conditions result in gelation since it is the initial formation of a three-dimensional crosslinked network. As a result, the resin can no longer flow, which prevents any further processing. Most epoxy matrix/resin that has been cured at room temperature halt at this point. When curing conditions (temperature, pressure, etc.) are met, vitrification takes place. For room temperature cured epoxy and their composites, gelation peaks in DMA might not show up since the phenomena were already subdued when the matrix reached topological stability, however, vitrification peak manifestation in damping factor (Tan **δ)** plots can be noticed.

3.5.1. Storage modulus ($E^{'}$)

The energy stored and matrix stiffness can be ascertained directly from the storage modulus (E'), which is a representation of the elastic response of a viscoelastic material. It has a substantial connection with the material's load-bearing capability. It can be related to flexural modulus when measured in three-point bending mode at room temperature (according to ASTM D790) [76]. As seen in Fig. 12**a**, the nanofillers played a significant role in improving the storage modulus (E') of the polymer matrix. The storage modulus (E') at different temperatures is reported in Table 3. The E' for EP, EM1, ES2 and ESM3 at room temperature was found to be ~ 2.80, 3.06, 3.41 and 3.44 GPa, respectively. The epoxy chains and MWCNTs develop a large interfacial area through entanglement interaction, which can be the reason for the rise in modulus for EM1 [21].

Lowering the molecular mobility of the polymer chains in the matrix through the higher aspect ratio of CNTs and their bridging effect can enhance the composite's elastic response. ES2 displayed the highest E' at room temperature. This can be attributed to the curing nature discussed previously where the crosslinking density increases drastically with a decrease in the cure time. SiN can bring the whole system closer to vitrification temperature thereby increasing the glassy and rigid nature of the composite. For room-temperature cured EP, the curing process stops at the upper gelation phase thereby displaying rubbery behaviour with lower E'. ES2, with higher crosslinking density as well as vitrification, exhibits a drastic increase in E`. The synergistic effect of dual nanofillers can be noticed in ESM3 where the E' increased significantly. This can be attributed to the curing nature of SiN and the entanglement of CNTs with the matrix.

Based on the kinetic theory of rubber elasticity [77], the curing density (ϑ_c) was computed, using Eq. (3), based on the moles of an elastically effective network of polymeric chains per unit volume [78].

Table 3
Storage modulus, damping factor and T_g for epoxy nanocomposites and hybrid nanocomposites.

Sn. No	Sample	E' at 27 °C (MPa)	E' at 50 °C (MPa)	Tan δ	T_g (°C)
1	EP	2800.58	2664.64	1.16	82.5
2	EM1	3066.71	2903.40	1.10	87.1
3	ES2	3444.66	3390.71	0.99	95.2
4	ESM3	3417.93	3223.72	0.75	90.4

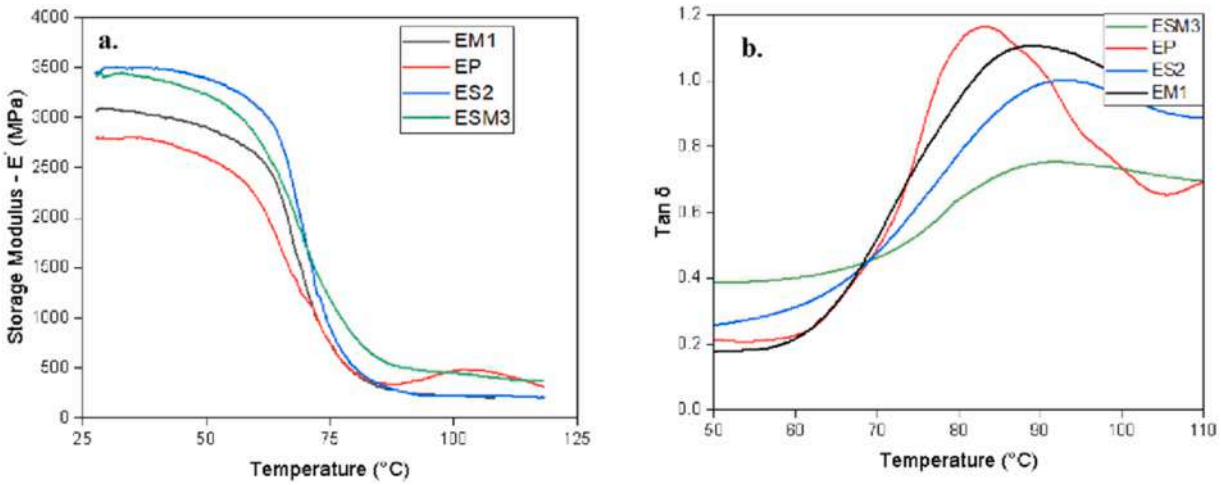

Fig. 12. Variation of a. storage modulus and b. Tan delta (δ) with temperature for epoxy, nano and hybrid nanocomposites.

$$\vartheta_c = \frac{E'}{3gRT} \quad (3)$$

Where, E' is the storage modulus of the epoxy, nanocomposites and hybrid nanocomposites obtained from the DMA curve at temperature T (K). R is the universal gas constant and g is the front factor related to the functionality of the resin ($g = 1$ for DGEBA) [78]. The variation in curing density at different temperatures is shown in Table 4. ES2 demonstrated improved curing density and elastically effective networks at room temperature due to their ability to distribute heat generated during curing which may induce vitrification uniformly. The increase in elastic network and crosslinking in the case of ESM3 was related to the presence of SiN and the dilution phenomenon for MWCNTs.

3.5.2. Tan δ

Tan δ is directly connected to the loss of mechanical properties and represents the ratio of the loss modulus (E'') to the storage modulus (E') [79]. A polymeric material's balance between its viscous and elastic phases is determined by its tan δ or damping behaviour. The filler's or polymers' interphase energy dissipation in a polymer composite is represented by its peak height. In polymer composites, the internal rubbing or friction resulting from the movement of polymer chains can be effectively judged by the peak value of tan **δ**. T_g is shifted to higher temperatures and tan **δ** 's peak value decreases if the nanofiller's dispersion and interaction in the matrix are excellent [80]. Excessive mobility of chain segments can increase internal friction thereby increasing the loss modulus. The damping values and peaks can be seen in Table 3 **and** Fig. 12**b**. EP showed the highest tan δ of ~ 1.16 and the lowest T_g of 82.5 °C. This mobilization of polymeric chains and improper curing which retained the viscous phase played a crucial role in increasing damping and displaying lower glass transition temperature. The presence of nanofillers in the matrix resulted in a decrease in tan δ height and a shift to the right in the glass transition temperature. Tan δ peak values are known to decrease when nanofillers are added to the matrix [81]. The enhanced peak broadening observed in nanocomposites and hybrid nanocomposites indicates exceptional relaxation characteristics, signifying optimal energy absorption during deformation. As SiN plays a crucial role in curing, the polymer chains are prevented from moving or slipping leading to a significant increase in T_g. From this, we can conclude that crosslinking density is inversely proportional to the degree of molecular mobility. The incorporation of SiN and MWCNT in ESM3 displayed a drastic decrease in tan δ height due to the combined effect of, a strong interface generated by MWCNT and an increase in crosslinking and secondary bonding due to SiN.

The prevention of molecular mobility of polymer chains in constrained zones can be determined from the energy loss fraction (W). The relation between energy loss fraction (W) for polymer nanocomposites with tan δ can be determined by equation [78]. Lower W values indicate lower energy loss in the system and can be directly correlated with the polymer-filler interaction. The W values, calculated from Eq. (4), for EP, ES2, EM1 and ESM3 are given in Table 4.

$$W = \frac{\pi * \tan\delta}{(\pi * \tan\delta) + 1} \quad (4)$$

The adhesion efficiency between polymer and nanofillers can be determined from tan δ peaks. The adhesion factor (A) can be found from the tan δ curve according to Eq. (5) [78]

$$A = \left(\frac{1}{1-\varphi_f}\right) * \left(\frac{\tan\delta_c}{\tan\delta_p} - 1\right) \quad (5)$$

Where,$\tan\delta_c$, $\tan\delta_p$ and φ_f are the damping peak values for composite, polymer and volume fraction of filler, respectively. The filler volume fraction for hybrid nanocomposite is taken as the sum of individual nanofillers with their according to wt%. Adhesion factor (A) values are given in Table 4. Improved and lower adhesion values indicate better filler-matrix interfacial adhesion interaction. The adhesion values decreased for ES2 and hybrid drastically showing better interactions and bonding thereby hindering chain mobility.

3.6. Creep analysis

The viscoelastic behaviour of polymers and their composites can be influenced by the gradual reorganization of polymer chains and molecules post stress-strain cycles [82]. Higher loads or elevated temperatures have the potential to speed up this rearranging process. For polymer-based materials, creep is a kind of viscoelastic or viscoplastic reaction in which strain is seen as output over time after the specimen is subjected to a static load as input. The inclusion of nanofillers can delay this process by preventing the mobility and slippage of chains. Thermosetting polymers, like EP, display superior creep resistance when compared to their thermoplastic counterparts due to their crosslinked structure. Room temperature cured EP has remnants of unreacted functional groups present in the system which reduces the crosslinking degree and efficiency. Tensile creep studies were conducted for EP, EM1, ES2 and ESM3 under a load of 50 Kg at 60 °C for 600 s (10 min). The creep rate in steady state or critical creep rate (CCR) was calculated from Eq. (6) and presented in Table 5.

$$\textit{Critical creep rate } (CCR) = \frac{\Delta\varepsilon}{\Delta t} \quad (6)$$

Materials generally undergo three main stages of creep, as illustrated in Fig. 13**b**: Initial/primary creep, Secondary/steady-state creep, and Tertiary creep. In the primary creep stage, minimal stretching occurs under loading. The secondary stage sees the material reaching stability, with a uniform strain rate as polymer chains rearrange in the direction of load. Cracks and voids may form due to elongation and stress concentrations. During tertiary creep, the material elongates exponentially, with crack and void accumulation leading to potential failure. Due to its brittle and thermosetting nature, EP exhibits a lower creep strain rate but is less effective at preventing crack initiation and propagation due to increased free volume. Fillers of various sizes and shapes are used to reduce free volume and crack propagation.

From Fig. 13**a**, it can be seen that the EP matrix fails quickly with a small steady-state region and significantly high CCR forming a plateau. The formation of the plateau region is due to the crack propagation as shown in Fig. 14**a** indicating the propagation of cracks leading to failure. The inclusion of MWCNTs delayed the creep response and can be

Table 4
Crosslinking density and adhesion factor for epoxy-based nanocomposites and hybrid nanocomposites.

Sn. No	Sample	ϑ_c at 27 °C	ϑ_c at 50 °C	ϑ_c at 60 °C	W	A
1	EP	374.27 * 10^3	330.75 * 10^3	267.18 * 10^3	0.78	–
2	EM1	409.81 * 10^3	360.39 * 10^3	317.67 * 10^3	0.77	−0.051
3	ES2	460.46 * 10^3	420.91* 10^3	376.18 * 10^3	0.75	−0.172
4	ESM3	454.78 * 10^3	400.18 * 10^3	340.65 * 10^3	0.70	−0.616

Table 5
Uniaxial tensile critical creep rate (CCR) for epoxy nanocomposites and hybrid nanocomposites.

Sn. No	Sample	Critical creep rate (1/min)
1	EP	6.62
2	EM1	2.29
3	ES2	0.07
4	ESM3	0.31

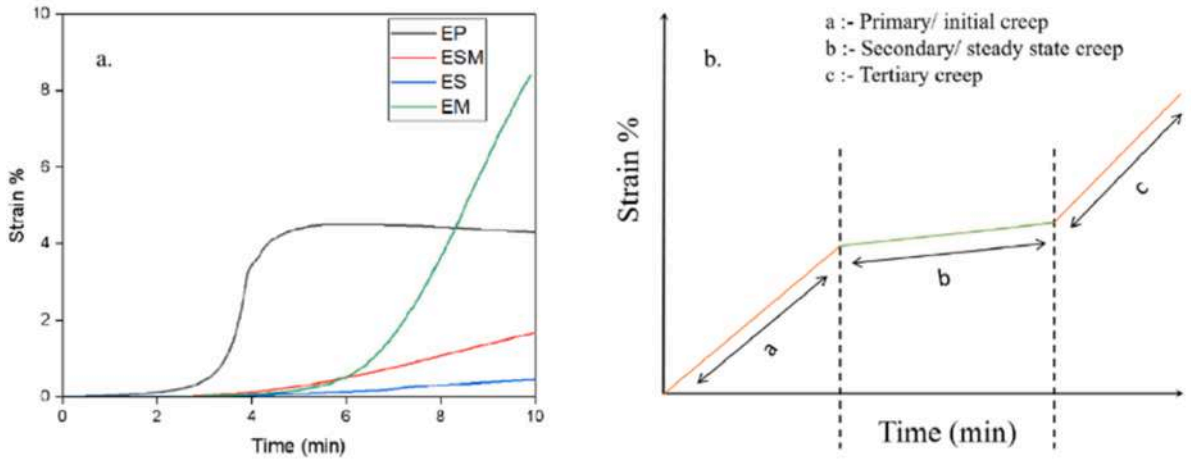

Fig. 13. Viscoelastic studies for epoxy nanocomposites and hybrid nanocomposites; a. Creep rate for EP, EM1, ES2 and ESM3 and b. Ideal creep curve for materials.

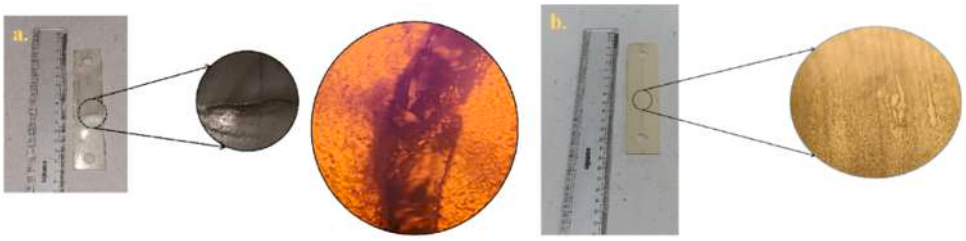

Fig. 14. Crack propagation of creep tested samples for a. EP b. ES2 after 10 min at 60 °C.

attributed to excellent interaction between filler and matrix. The secondary region is significantly more pronounced than EP with a comparatively low CCR indicating polymer chain slippage due to the self-lubricating effect of CNTs. The strong bridging effect of CNTs prevented crack propagation and was noticed in our earlier studies where the inclusion of CNTs significantly improved fracture toughness [11].

ES2 displayed the lowest CCR with a delayed primary stage and no visible damage to the specimen, as shown in Fig. 14**b**. This noteworthy resistance to creep can be credited to the sharp increase in crosslinking density and formation of strong secondary bonds with the matrix which prevented the rearrangement and mobility of polymer chains at elevated temperatures and loading. ESM3, being a combination of properties of ES2 and EM1, displayed slightly higher CCR than ES2 but lower than EM1 and EP. The lower CCR can be accredited to the efficient and speedy curing provided by SiN and the prolonged steady state region can be accredited to the lubricating and bridging effect of MWCNTs.

The notable improvement in the mechanical properties of epoxy with the inclusion of the dual filler system can be attributed to the synergism between the dual nanofillers. The bridging/ stitching mechanism provided by MWCNTs delays the crack propagation caused by voids and defects [22,74], as seen in Fig. 15**a**, while the strong interaction of the -COOH groups with the polymer matrix enhances the static, dynamic

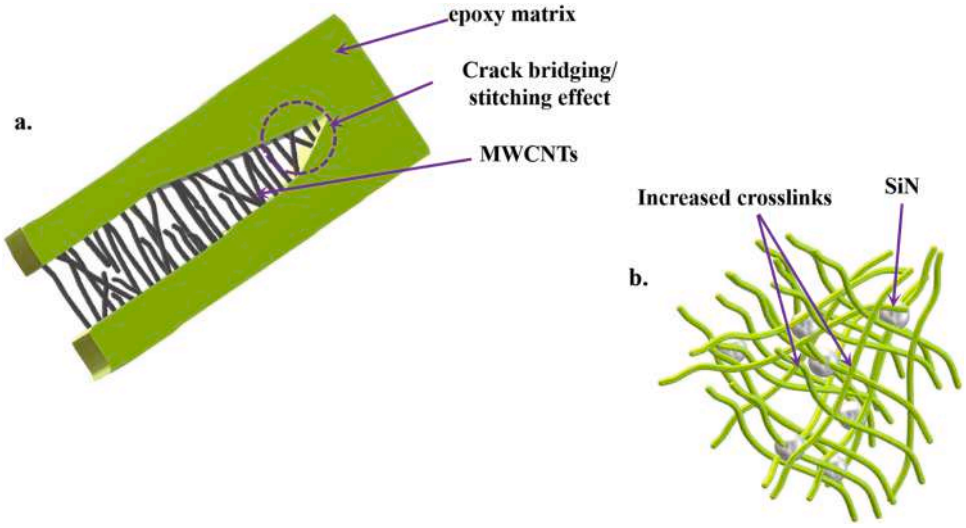

Fig. 15. Enhancement of mechanical properties by a. bridging effect or stitching effect of MWCNTs and b. increased crosslinking density of EP by incorporation of SiN.

mechanical and viscoelastic performance. Additionally, the significant increase in crosslinking density, resulting from incorporating nano SiN, (as reported in Section 3.2 and seen in Fig. 15**b)**, substantially enhances the matrix's stiffness and stability. This leads to improved storage modulus, flexural modulus and T_g, as interpreted from DMA, and creep studies. The synergistic interaction between these two fillers was particularly evident in the hybrid nanocomposite system, where the combined effects of increased crosslinking density and the MWCNTs bridging mechanism enhanced the overall mechanical properties, even at low nanofiller content.

3.7. Corrosion behaviour

The coating efficiency and anticorrosion properties were evaluated using electrochemical impedance spectroscopy (EIS). The utilization of frequency-dependent impedance measurements represents a valuable technique for the systematic assessment and surveillance of barrier coatings' degradation within coating/ metal systems. Through this method, the double-layer capacitance and charge transfer resistance, the important parameters delineating the interfacial characteristics of the coating proximal to the metal substrate, can be reliably ascertained. This analytical approach affords a comprehensive insight into the evolving nature of the coating system under varied environmental conditions, thereby facilitating a meticulous comprehension of degradation mechanisms and informing targeted mitigation strategies [83]. The coating barrier properties, water absorption, defect presence, interface reactivity, coating adhesion, coating delamination index, coating damage index, and breakpoint frequency can be analyzed using EIS [84]. It can monitor the deterioration/ swelling of polymeric coatings exposed to electrolytes. The main advantage of EIS for polymeric coatings is that it's non-destructive and can be used to study the regeneration of films. As illustrated in Fig. 16**,** the samples EP, EM1, ES2, and ESM3 were exposed to cyclic corrosion or corrosion fatigue after keeping them immersed in a 3.5 % NaCl solution for two days at a temperature variation of 40 °C to −3 °C at 1 °C/ min heating rate and 70 % relative humidity.

With the aid of EIS tests, the corrosion properties of MS coated with EP, EM1, ES2, and ESM3 were ascertained. Figs. 17**a,** 17**b and** 17**c** show the resulting Nyquist plot and Bode plots. Figs. 17**d,** 17**e, and** 17**f,** respectively, display the models that were used to fit EP, MS, and composites. R1 is the solution resistance, while R2 and C2 are the resistance and capacitance for the corrosion product layer and surface pores, respectively, based on circuits shown in Figs. 17**d and** 17**f**. The constant phase element (Q) can be defined as capacitance which is independent of frequency. Q3 and R3 are coating capacitance and resistance, and Q4 and R4 are double-layer capacitance and charge transfer resistance, respectively. Charge transfer resistance is an important parameter which can determine the overall corrosion resistance of the coating and is inversely proportional to the rate of corrosion [85].

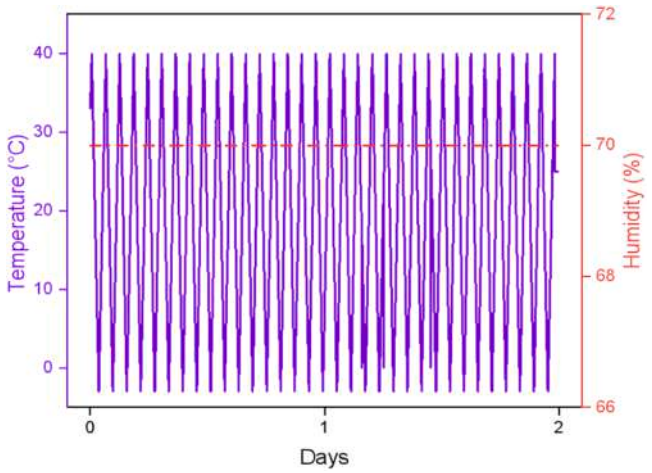

Fig. 16. Cyclic corrosion condition for coatings.

In the case of the MS sample, the circuit model shown in Fig. 17**e** follows a corroded sample's equivalent circuit model [86] where R1 is the solution resistance, while C1 and R2 are the capacitance and resistance for the corroded product layer and surface oxidation, and R3 and Q3 being resistance to charge transfer and double layer capacitance respectively. The values obtained for coatings and MS are listed in Table 6 **and** Table 7**,** respectively.

From Table 7**,** it can be noticed that MS displayed the lowest resistance to the corrosive solution indicating the inability of the material to withstand corrosive attacks. The formation of oxides as seen in R2 and C1 and the presence of double-layer capacitance and lower charge transfer resistance from Table 7 indicates that the metal has undergone corrosion. The maximum charge transfer resistance and the lowest double-layer capacitance were displayed by ES2. Due to SiN's exceptional hydrophobicity [87], the corresponding nanocomposite displays resistance to the absorption of electrolytes. The ceramic material's insulating properties are responsible for the high charge transfer resistance. The capability of SiN to resist diffusion of water and sodium [88] enables ES2 to manifest excellent corrosion resistance to cyclic corrosion in NaCl electrolytes. A perfect resistor won't allow the flow of electrons/ current within the system, and will not manifest any phase angle whereas a perfect capacitor displays a phase angle of −90°, due to current lag during the voltage drop. The increase in the flow of charges or decrease in impedance for polymer coatings can be accredited to the defects or damages on the coatings due to chemical reactions, as well as the swelling due to water and electrolyte absorption rendering it conductive. The material's hydrophobicity and chemical inertness play a vital role in such instances.

Phase angles vs freq. plots can be crucial in understanding the corrosion mechanisms in the case of polymer coatings. From Fig. 17**c**, it can be noticed that the initial phase angles at low frequencies are high for EM1, EP and ESM3 whereas ES2 and MS displayed relatively low phase angles. EP displayed the highest phase angle of ~ −35° followed by EM1 and ESM3 with ~ −33° and ~ −29°, respectively indicating capacitive behaviour due to the presence of defects, increased surface area and a possibility of electrochemical reactions. These properties can generate double-layer capacitance on the surface creating a phase lag thereby showing higher phase angles. The drop in phase angle with an increase in frequency can be due to the resistive nature. This is an indication of, ease of charge transfer and charge transfer reactions occurring at the metal-electrolyte interface suggestive of an increase in corrosion rates due to the thinning of the passive layer formed on the coating surface. The swelling of the coating can also result in creating conductive pathways responsible for decreasing the phase angle at higher frequencies. The decrease in phase angle for ESM3 at low frequency can be attributed to the presence of SiN leading to a sharp increase in crosslinking density, reduction in defects and the formation of a protective layer, whereas a steep fall of phase angle at high frequency can be attributed to the charge transfer reactions and conductive nature possible due to the presence of CNTs. ES2 being hydrophobic and chemically inert prevented the water and electrolyte uptake in the coatings. The ES2 sample displays ~ −12° phase angle at low frequency exhibiting resistive behaviour due to the formation of thin layers of silica [89,90] and the ability of SiN to form a barrier [45]. These layers prevent the diffusion of corrosive ions through the coating manifesting resistance to water and electrolyte swelling. A noticeable loss in phase angle at a higher frequency is absent in the case of ES2 assigned to uniform and stable properties throughout its structure. The constant phase angle is due to the resistance against charge transfer between metal and electrolyte contributing to overall corrosion resistance. An increase in phase angle from ~ −12° to ~−18° can be considered as proof for its capacitive behaviour. Two distinct time constants can be seen in the case of ES2 (Fig. 17**c)** indicating two complex relaxation phases. The first relaxation phase suggests the formation of passive and

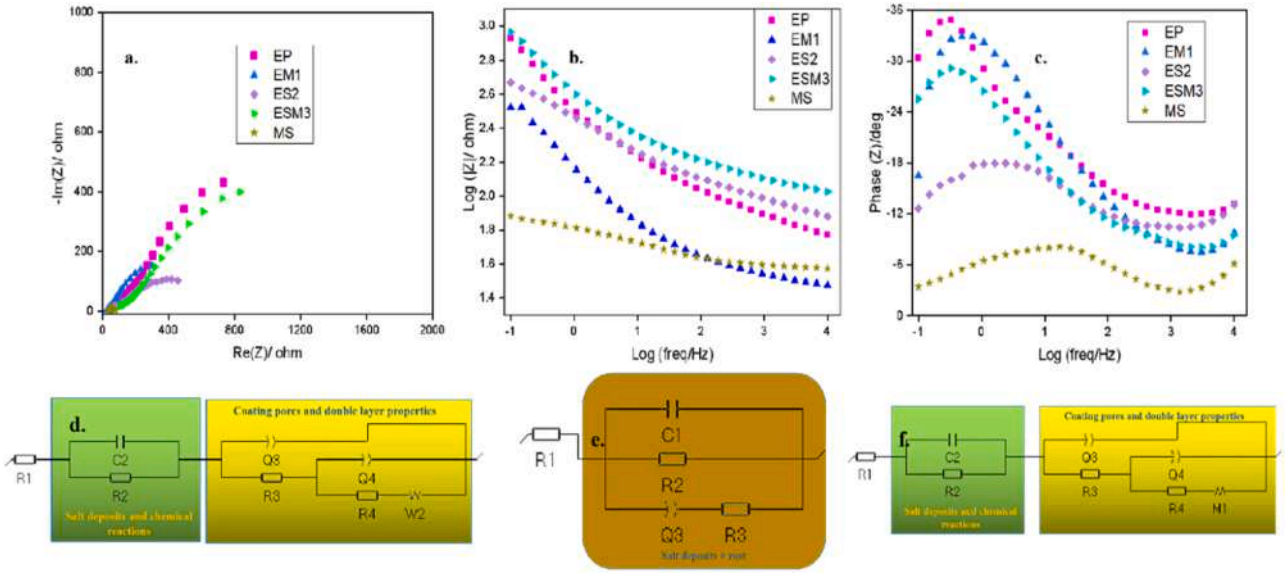

Fig. 17. EIS corrosion analysis of coatings; a. Nyquist plot, b. and c. Bode plots, d. equivalent circuit for nanocomposites, e. equivalent circuit for MS and f. equivalent circuit for EP.

Table 6
Resistance and capacitance values obtained for coatings from the equivalent circuits.

R (Ω)/ C (F)	EP	EM1	ES2	ESM3
R1	3.487	1.656	40.12	O.2017
C2	3.086×10^{-3}	4.556×10^{-3}	0.505×10^{-6}	4.01×10^{-3}
R2	441.2	181.7	19.47	294.4
Q3	14.89×10^{-6}	0.354×10^{-3}	1.92×10^{-3}	1.136×10^{-3}
R3	54.5	36.92	412.5	197.4
Q4	2.421×10^{-3}	1.38×10^{-3}	0.111×10^{-3}	0.867×10^{-3}
R4	42.36	220.5	430.1	60.41

Table 7
Resistance and capacitance values obtained for MS sample from the equivalent circuit.

R (Ω)/ C (F)	MS
R1	16.19×10^{-12}
C1	36.56×10^{-9}
R2	81.05
Q3	1.74×10^{-3}
R3	67.56

protective layers whereas the second relaxation at a higher frequency can be attributed to the repairing of protective layers. Such coatings are more desirable as they have more efficacy in protecting MS for longer durations. A distinct phase angle at a lower frequency can be due to the formation of protective films or oxide layers [86]. In the case of MS, the sinusoidal phase at low phase angles can be correlated with the formation of oxides on the surface. Two-time constants can be seen in the case of MS as well. The peak at a higher frequency can be assigned to the formation of oxides and a low phase angle at higher frequencies can be related to the charge transfer responsible for corrosion.

From Fig. 17**b**, the samples ESM3, ES2 and EP display higher |Z| at lower frequencies denoting resistance against charge transfer and passive film formation whereas EM1 displayed slightly lower |Z| due to the conductive nature of CNTs and improper formation of passive films on the coating surface. As the frequency increases, |Z| values of EP and EM1 drop drastically owing to the loss of resistance against the diffusion of corrosive ions. ESM3 and ES2 didn't display a significant loss in |Z| indicating superior corrosion resistance. The ES2 sample's passive film regeneration as seen from its phase angle plot can be decisive in stabilizing the |Z| at higher frequency. A sharp drop in |Z| and phase angle can be noticed as frequency increases for EM1 in Figs. 17**b and** 17**c,** which can be attributed to the chemical reaction between the -COOH functional group of MWCNT with NaCl in the electrolyte which creates pathways for corrosive ions via pitting and degradation.

Coating protection efficiency (%CE) is calculated using Eq. (7) [91]

$$\%CE = \frac{R_{coat\ with\ NP} - R_{coat\ without\ NP}}{R_{coat\ with\ NP}} \quad (7)$$

Where $R_{coat\ with\ NP}$ is the coating resistance of nanocomposites and hybrid nanocomposites and $R_{coat\ without\ NP}$ is the resistance of the matrix. From equation [7], it was found that ES2 gave the highest CE% of ~87 whereas EM1 gave the least CE% of ~ −48 indicating a high corrosion rate under fatigue cycles.

3.7.1. *Polymer corrosion mechanism*

Since metals corrode due to an electrochemical reaction, their corrosion mechanism can be predicted. Polymers don't corrode at different rates like metals do since they either degrade quickly or remain inert to chemicals. When solvent attack occurs, corrosive material penetrates the polymers or plastics, causing swelling, softening and eventual failure [92]. By the nature of attacking methods, plastic corrosion can be classified as degradation brought on by permeability, absorption, and other causes; attacks on ester links during hydrolysis and chemical bonds during oxidation, respectively; depolymerization through thermal degradation, radiation, or a mix of these processes [92]. Delamination, crazing, softening, dissolving, discolouration, or swelling may ensue from these features. In the case of thermosets, like epoxy, curing is of utmost importance as improper curing can reduce chemical resistance of the polymer, whereas proper curing will result in excellent chemical resistance. Since polymers have permeability that is orders of magnitude larger than that of metals, permeability plays a critical role in the failure of the polymer matrices. Molecular migration through voids, fissures, or flaws that are present in the polymer surface or the chains of the polymer is known as permeability. Despite its destructive nature, permeation is solely a physical phenomenon [92]. Two factors which directly influence the permeation of corrosive elements into the matrix are diffusion through the polymer chains and the other being the solubility of corrodant in the polymer. The migration of corrosive ions into the coating can be accelerated by partial pressure

created in the system by periodic temperature changes during corrosion fatigue. As a result, a few variables, including coating thickness, permeant concentration, temperature, and pressure, can be adjusted to control permeant movement in the coating. As the solubility of the permeant in the matrix increases owing to the polymer chain movement allowing accelerated diffusion of corrosive ions, an increase in temperature might raise the permeation rate.

An increase in crosslinking density can guarantee a decrease in ion diffusion through the coating, enhancing its ability to resist corrosion. The permeant's slow condensation rate, high intermolecular interactions, higher crystallinity, higher degree of crosslinking, permeant size, and chemical similarity between the polymer and permeant are other factors that can lower the penetration rate. Accordingly, fillers are used to reinforce polymers to decrease the amount of corrosive ions that penetrate the system and, consequently, the number of voids and flaws. Fillers, particularly nanofillers, can slow down the diffusion of corrodents, which lowers the rate of corrosion. An unfilled thermoset often experiences chemical and physical corrosion, with physical corrosion being reversible like swelling or water absorption. Physical corrosion can alter the properties of the coating but no chemical reactions take place. Chemical corrosion is irreversible because it attacks bonds directly and causes failure at the molecular level. Therefore, it is essential to incorporate fillers which are chemically inert and preferably hydrophobic to reduce the tendency of the matrix to corrode. Ideally, MS corrodes rapidly along with rust formation with several steps of oxidation and reduction reactions when exposed to NaCl electrolyte. The reactions occurring in the corrosion of MS are shown below [37].

$$Fe \rightarrow Fe^{2+} + 2e^{-} \quad (1)$$

$$O_{2(g)} + 2H_2O + 4e^{-} \rightarrow 4OH^{-} \quad (2)$$

$$Fe^{2+} \rightarrow Fe^{3+} + e^{-} \quad (3)$$

$$2Fe^{2+} + 2H_2O + O_{2(g)} \rightarrow 2FeOOH + 2H^{+} \quad (4)$$

$$Fe + NaCl_{(aq)} \rightarrow FeCl_2 + NaOH \quad (5)$$

Steel starts to rust only when sufficient oxygen, water, or moisture is present. In this instance, rapid reactions could be brought on by thermal straining and fast NaCl condensation rates, which would hasten MS corrosion as shown in Fig. 18. Therefore, MS is coated with EP and its nanocomposites to prevent its rusting. In this work, MS is coated with EP, EM1, ES2 and ESM3 and their corrosion mechanisms are studied.

Concerning different coatings and their interactions, it is crucial to understand that remnants, such as amine hardeners, appear in room-temperature cured EP and its composites. These remnants can participate in chemical reactions with corrosive NaCl, as illustrated below [93].

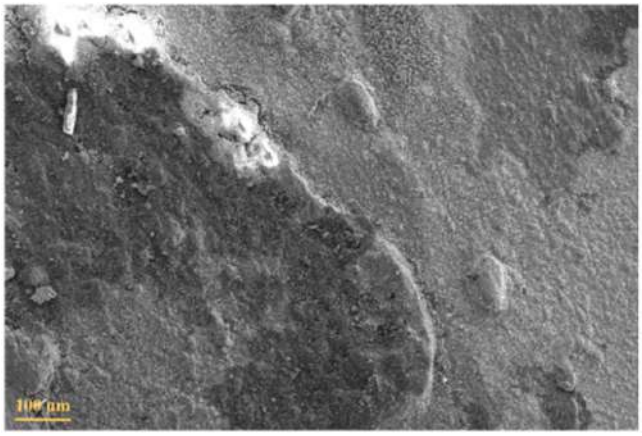

Fig. 18. FESEM image of corroded MS sample.

$$R - NH_2 + NaCl \rightarrow R - NHNa + HCl \quad (6)$$

$$R - NH_2 + 2O_2 \rightarrow R - NO_2 + H_2O_2 \quad (7)$$

$$R - CONH_2 + NaCl \rightarrow R - CONa + HCl + H^{+} \quad (8)$$

$$R - CONH_2 + H_2O \rightarrow R - CHO_2 + R - NH_2 \quad (9)$$

In the case of EP coating, due to cyclic thermal variation and the presence of corrosive ions along with high relative humidity, a high number of pits and surface cracks formed can decrease tortuosity as seen in Fig. 19**a.** These defects act as a pathway for corrosive ions like Cl^{-} and O^{2-} thereby promoting corrosion of the metal. Additionally, warpages were observed which suggests that the specimen's constant heating and cooling along with swelling produced distortions on the coating's surface. These deformities may serve as stress concentration sites where corrosive media may penetrate, creating pits or fissures. Furthermore, salt deposits were seen in Fig. 19**a**, suggesting that EP was unable to halt or postpone the nucleation of NaCl during the cooling phase. These salts can disintegrate the material gradually from the inside and cause crevice corrosion, which deteriorates the material's qualities. For EM1, few chemical reactions are possible which can damage the specimen thereby decreasing the tortuosity of the coating. In EM1, the matrix is reinforced with COOH-MWCNT where the -COOH functional group can take part in chemical reactions with NaCl as shown below.

$$R - COOH + NaCl \rightarrow R - COONa + HCl \quad (10)$$

It was found that COOH-MWCNT doesn't play an appreciable role in improving the crosslinking of the matrix indicating that the number of remnants is high. From reactions (6)-(10), we can deduce that a high amount of hydrochloric acid (HCl) has been generated from the severe corrosive reactions. This increases the corrosion rate of the coating thereby increasing pittings and defects. As seen in Fig. 19**c**, the formation of larger pits is evidenced which can be credited to the corrosive environment created by this coating. Blisters and pore warpages were also observable due to the absorption of water and electrolytes. This can be attributed to the hydrophilic nature of COOH-MWCNT which can attract water into the coating [94]. In the case of ES2, it was well established that SiN improves the crosslinking density of the matrix which decreases the overall remnants in the system as well as generating strong secondary bonds with the polymer chains. Higher crosslinking density improves the corrosion resistance of the thermoset materials [92]. Along with the improvement in curing, SiN being chemically inert, electrically insulative and highly hydrophobic, makes it an ideal nanofiller to boost corrosion resistance. This can be corroborated from Fig. 19**b** where the size and number of pits are comparatively less due to the absence of reactions(6)-(9). Blisters or NaCl deposits are not visible indicating perfect hydrophobicity and chemical inertness of ES2. In ESM3, as seen in Fig. 19**d**, a combination of SiN and COOH-MWCNT's properties can be anticipated. The size of pores is less owing to the chemical inertness of SiN but a high wt% of COOH-MWCNT in the system led to a sharp increase in blisters and warpages in the coating.

Figure S3 shows the energy dispersive x-ray (EDAX) with colour mapping images for MS, neat matrix, nanocomposites and hybrid nanocomposites. EDAX showed complete consumption of N in the system for all composites indicating the occurrence of amine and amide reactions with the electrolyte. Salt deposits are seen in **Figures S3c and S3d** for EM1 and ESM3 demonstrating the reaction between NaCl and COOH functional groups which led to the corrosion of the substrate along with the NaCl deposition on the surface and in the pits. These depositions can lead to the deterioration of the coating over a long period. Rusting or oxidation of MS can be seen in **Figure S3e**.

The tortuosity of the coatings can be determined with the help of BET analysis where nitrogen gas is plunged into the pores and the volume occupied by the pores is found. From Fig. 20, it is observed that ES2 displayed the lowest volume intake whereas EP recorded the highest

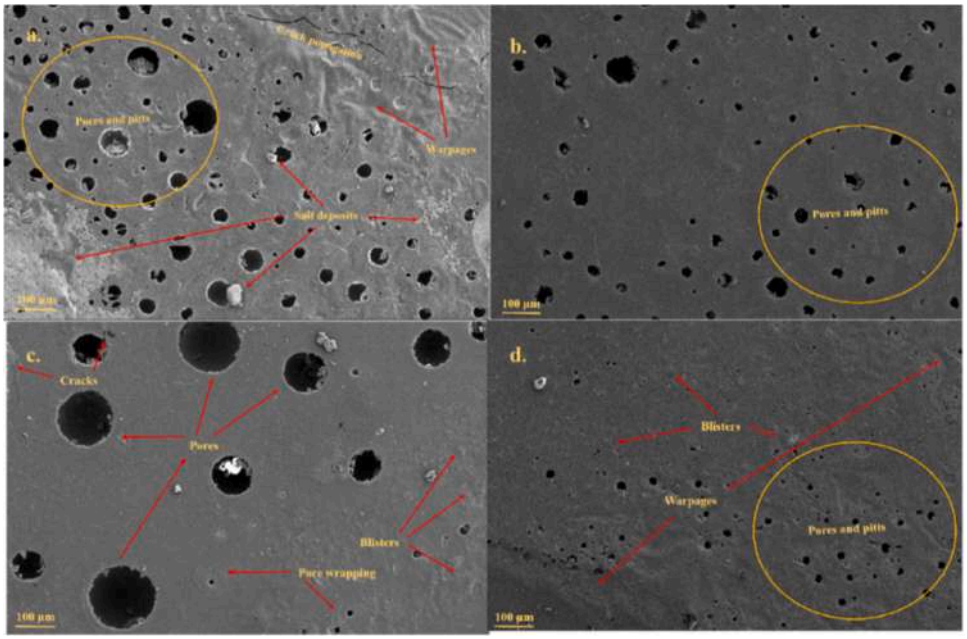

Fig. 19. FESEM images of coatings after corrosion test a. EP, b. ES2, c. EM1 and d. ESM3.

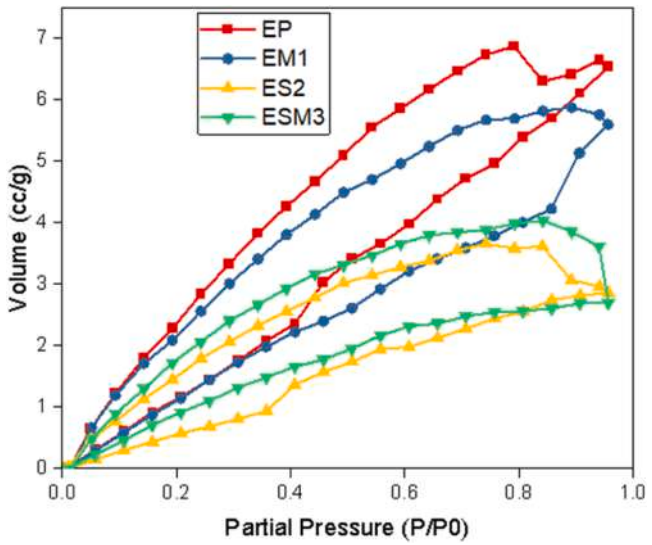

Fig. 20. Physisorption isotherms of Nitrogen gas (BET) for EP, EM1, ES2 and ESM3.

volume intake. The total volume for pores less than 234.5 Å (radius) at P/P0 for EP, EM1, ES2 and ESM3 was found to be $1.012e^{-2}$, $8.864e^{-3}$, $4.420e^{-3}$ and $4.175e^{-3}$ cc/g, respectively. By arranging the samples in ascending order of volume intake, it can be represented as ES2 < ESM3 < EM1 <EP. A small amount of steam is absorbed by the liner as a result of the temperature and pressure gradient during thermal cycling, and eventually condensing to water inside the inner wall during the cooling phase. The confined water may expand to vapour upon pressure release or the introduction of steam, creating a first micropore. The liner eventually develops noticeable blisters filled with water as a consequence of the repetitive pressure and heat cycling, thereby expanding the pores [92]. SiN is known to uniformly distribute heat throughout the system, thereby reducing thermal shock and pressure difference in the coating and reducing the chances for the formation of micropores. The lowest volume intake for ES2 indicates a lack of interconnected pathways which prevents the diffusion of corrosive ions and water to the metal surface. EP being an unfilled thermoset has the lowest resistance to thermal shocks and partial pressure gradient which may generate pores and cracks leading to the possibility of crevice corrosion. EM1 displayed lower volume intake when compared to EP, but almost 3 times more than ES2. This can be attributed to the hydrophilicity of COOH-MWCNT which attracts water, and the reaction between NaCl and COOH which generates HCl. This corrosive acid is largely responsible for the number and depth of pores generated. The reduction in volume intake for ESM3 can be attributed to SiN's chemical inertness and hydrophobic behaviour, which reduced the depth of pits.

3.8. *Electromagnetic interference (EMI) shielding*

When a magnetic field and an electric field perpendicular to each other come into contact, electromagnetic (EM) waves are produced. The term EM radiation describes the electromagnetic waves that travel through space-time and carry radiant energy [95]. Electromagnetic interference (EMI) shielding is a technique that creates a barrier to prevent leakage of strong electromagnetic fields that can interfere with sensitive devices and signals. Based on their respective contributions to the overall shielding, EMI shielding materials can be categorized as either absorption-dominant or reflection-dominant. Two basic mechanisms are responsible for the attenuation of EMI shielding: primary and secondary. The primary kind of shielding is reflection, which is achieved by either reflecting from the shield's surface or its opposite side, by establishing an impedance discontinuity at the air/shield boundary. Absorption is the secondary method in which electromagnetic radiation (EM) is transformed into thermal energy and transmitted through a material. CNTs are a typical example of EM absorbers [96]. EP, EM1, ES2 and ESM3 composites were characterized using a two-port setup using a coaxial waveguide adaptor at X-band frequency range as shown in Figs. 21**a and** 21**b**. The total shielding effectiveness, SE_{total}, was calculated by the addition of shielding effectiveness due to reflection, SE_R, and shielding effectiveness due to absorption, SE_A, as expressed in Eqs. (7-9**)** where S_{11} and S_{21} are the parameters for reflection and transmission respectively [97].

$$SE_{total} = SE_R + SE_A \tag{7.1}$$

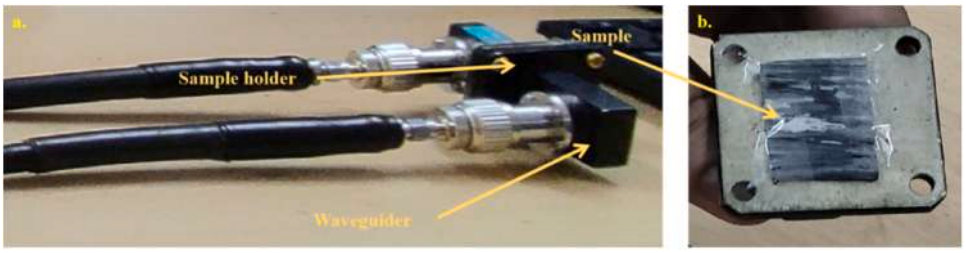

Fig. 21. Experimental setup for conducting EMI shielding tests on EP, EM1, ES2 and ESM3.

$$SE_R = 10\log\left(\frac{1}{1-R}\right) = 10\log\left(\frac{1}{1-|S_{11}|^2}\right) \quad (8)$$

$$SE_R = 10\log\left(\frac{1-R}{T}\right) = 10\log\left(\frac{1-|S_{11}|^2}{|S_{21}|^2}\right) \quad (9)$$

The scattering matrix provided by the VNA provides scope for computing SE_R and SE_A for the samples. These are calculated and provided in Fig. 23.

From the depicted results, it is evident that ES2 exhibits lower SE_R compared to EP, while the incorporation of conductive MWCNTs notably enhances SE_A for EM1 and ESM3. The imperative attribute of low reflectivity is of paramount significance, particularly in radar-evading applications, where reflections can undermine operational effectiveness. In this regard, SiN as a filler material emerges as a pivotal component. The mechanisms are pictorially presented in Fig. 22**.** The exceptional electrical conductivity of CNTs, combined with their EM waves absorption mechanism, remarkably enhance EMI shielding effectiveness. The nanotubes trap radiation through quantum confinement within their tubular structure, converting it into heat, while their high aspect ratio promotes multiple internal reflections, further delaying or absorbing incident waves. In contrast, the dielectric and non-magnetic nature of SiN, with minimal absorption and reflection capabilities, makes it ineffective for EMI shielding. As delineated in **Figures 23(a-c),** SiN is passive and do not hinder the shielding properties of MWCNTs, making it a valuable supporting filler in multi-filler systems that require superior EM shielding coupled with enhanced mechanical, thermal and corrosion resistance properties. The substantially reduced reflectivity of SiN-based composites, especially when compared with the EP matrix and when synergistically combined with exceptional absorbers like CNTs, underscores its potential in stealth-based applications.

4. Conclusions

In this study, epoxy composites were reinforced with a dual filler system comprising n-SiN and COOH-MWCNTs, fabricated using a lay-up method and cured at room temperature for 72 h. The investigation of wear and frictional behaviour using pin-on-disc equipment revealed that ES2 exhibited the lowest wear rate of 1.65 * 10^{-8} g/Nm due to SiN's ceramic nature. Increasing CNT content enhanced adhesion, forming transfer films and reducing COF sharply. ESM3 showed a minimum wear resistance of 2.07 * 10^{-8} g/Nm among hybrid nanocomposites, indicating synergy between dual nanofillers. Raman spectroscopy and FTIR demonstrated that SiN in the EP matrix at room temperature improved crosslinking density by uniformly distributing heat and promoting ring-opening mechanisms. DSC thermograms showed increased crosslinking density and decreased secondary cure time. Flexural tests in 3-point mode showed ES2 with the highest bending modulus and strength, improving it by ~30 % and ~200 % when compared with neat EP, attributed to high crosslink density. HR-TEM depicted uniform dispersion of dual nanofillers, enhancing stress transfer. DMA analysis showed a significant increase in storage modulus (E') by ~ 600 MPa with SiN nanofiller inclusion. ES2 displayed a notable ~13 °C increase in Tg compared to the neat EP matrix. It also exhibited the least creep rate due to increased crosslink density. EM1 showed a higher strain %, crediting the lubricating effect of CNTs.

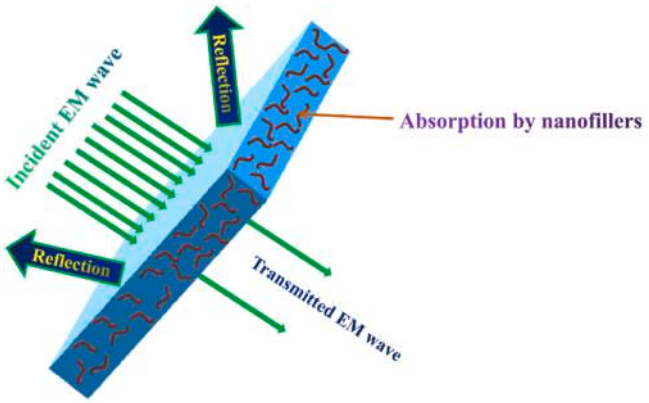

Fig. 22. Electromagnetic Interference shielding mechanisms.

ES2 displayed the highest corrosion fatigue resistance against 3.5 wt % NaCl medium with a coating efficiency of 87 %, forming a barrier/passive film to prevent corrosive ion diffusion. EM1 and ESM3 exhibited chemical reactions with NaCl and COOH functional groups on MWCNTs' surface whereas the ability of SiN to reduce excessive amine groups in the system is studied. Physisorption (BET) for corroded samples revealed that ES2 had the fewest pores and low nitrogen volume adsorption, indicating a lack of interconnected pathways which solidifies the high resistance against cyclic corrosion. EMI tests showed SiN had lower reflectivity than the base EP matrix and didn't hinder CNTs' absorbing behaviour, making them potential candidates as effective nanofillers for stealth applications in defence sectors.

Overall, the synergistic blend of SiN and COOH-MWCNTs showcased outstanding performance within the EP matrix. SiN demonstrated promising potential as a supportive nanofiller within multi-nanofiller systems, enhancing curing processes and structural integrity. Notably, ESM3 emerged as the optimal hybrid, offering versatility across different application sectors. It excelled particularly in coatings tailored for offshore environments characterized by severe corrosion and wear challenges. Additionally, ESM3 exhibited remarkable efficacy in providing high electromagnetic interference (EMI) shielding, making it a potential coating material for stealth-based defence sector applications.

Although this research highlights a range of multifunctional properties relevant to applications from composites to coatings industry, it is limited to the samples fabricated at room temperature. There is a significant potential for further studies involving different processing techniques like high temperature autoclave and vacuum assisted resin transfer molding (VARTM). Further investigation into the multi-filler systems combining SiN and other carbon-based nanomaterials, such as graphene, can be employed to explore their tribological behaviour, thermal performance and corrosion resistance.

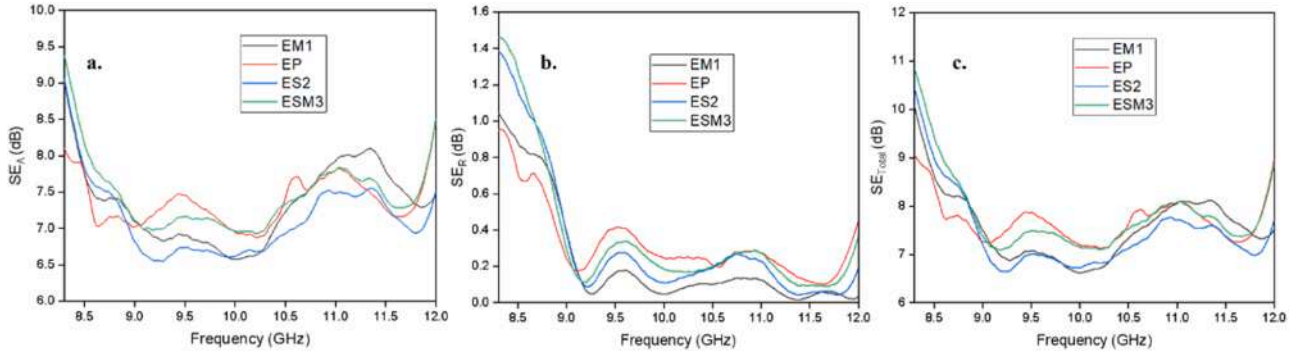

Fig. 23. EMI shielding effectiveness by a.SE_A, b.SE_R and c.SE_{total} plots for EP, EM1, ES2 and ESM3, respectively.

CRediT authorship contribution statement

Gopal krishna Bhagavatula: Writing – original draft, Methodology, Investigation, Formal analysis, Data curation, Conceptualization. **Snaha Leena:** Formal analysis, Data curation. **Kannan Murugasamy:** Formal analysis, Data curation, Conceptualization. **Rasana Nanoth:** Writing – review & editing, Supervision, Methodology, Investigation, Formal analysis, Conceptualization. **Sabarish Narayanan:** Formal analysis, Data curation. **Alessandro Pegoretti:** Writing – review & editing. **Jayanarayanan Karingamanna:** Writing – review & editing, Validation, Supervision, Project administration, Methodology, Investigation, Formal analysis, Data curation, Conceptualization.

Declaration of competing interest

The authors declare that they have no known competing financial interests or personal relationships that could have appeared to influence the work reported in this paper.

Acknowledgements

The authors extend their sincere appreciation to the Department of Mechanical Engineering, Amrita Vishwa Vidyapeetham, Coimbatore, for generously providing the necessary facilities and instruments for conducting the experiments. Additionally, the authors gratefully acknowledge the support received from the Center of Excellence for Advanced Materials and Green Technologies (CoE-AMGT), Amrita Vishwa Vidyapeetham, Coimbatore, for their assistance in material characterization. Special gratitude is also owed to the Department of Civil Engineering, Amrita Vishwa Vidyapeetham, for their support in facilitating electrochemical testing procedures. Furthermore, the authors express their heartfelt thanks to Ms. R. Sudha of the Microwave and Antenna Lab, Department of Electronics and Communication, Amrita Vishwa Vidyapeetham, Coimbatore, for her invaluable assistance and support during the EMI testing phase. The authors also extend their appreciation to MG University, Kottayam, India, for generously providing access to their HR-TEM characterization facility. Additionally, the authors acknowledge IIT Madras, Chennai, for granting access to their DMA testing facility.

Supplementary materials

Supplementary material associated with this article can be found, in the online version, at doi:10.1016/j.surfin.2024.105477.

Data availability

Data will be made available on request.

References

[1] R. Ghamarpoor, A. Fallah, M. Jamshidi, A review of synthesis methods, modifications, and mechanisms of ZnO/TiO_2 -based photocatalysts for photodegradation of contaminants, ACS Omega 9 (2024) 25457–25492, https://doi.org/10.1021/acsomega.3c08717.
[2] K. Baghitabar, M. Jamshidi, R. Ghamarpoor, Exfoliation, hydroxylation and silanization of two-dimensional (2D) montmorillonites (MMTs) and evaluation of the effects on tire rubber properties, Polym. Test. 129 (2023) 108265, https://doi.org/10.1016/j.polymertesting.2023.108265.
[3] R. Ghamarpoor, A. Fallah, T. Eghbali, Design of bifunctional sandwich-like Co@Si/Ox-MXene nanocomposite to increase the supercapacitor properties and removal of pollutants from wastewater, J. Alloys Compd. 983 (2024) 173920, https://doi.org/10.1016/j.jallcom.2024.173920.
[4] R. Ghamarpoor, A. Fallah, M. Jamshidi, Investigating the use of titanium dioxide (TiO2) nanoparticles on the amount of protection against UV irradiation, Sci. Rep. 13 (2023) 9793, https://doi.org/10.1038/s41598-023-37057-5.
[5] M. Neshastehgar, M. Jamshidi, R. Ghamarpoor, Self-assembly TiO2@Silane@SiO2 core-shell as s-scheme heterojunction photocatalyst against methylene blue degradation: synthesis and mechanism insights, J. Mol. Struct. 1319 (2025) 139406, https://doi.org/10.1016/j.molstruc.2024.139406.
[6] R. Ghamarpoor, A. Fallah, M. Jamshidi, S. Salehfekr, Using waste silver metal in synthesis of Z-scheme Ag@WO3-CeO2 heterojunction to increase photodegradation and electrochemical performances, J. Ind. Eng. Chem. 128 (2023) 459–471, https://doi.org/10.1016/j.jiec.2023.08.010.
[7] R. Ghamarpoor, M. Jamshidi, A. Fallah, F. Eftekharipour, Preparation of dual-use GPTES@ZnO photocatalyst from waste warm filter cake and evaluation of its synergic photocatalytic degradation for air-water purification, J. Environ. Manage. 342 (2023) 118352, https://doi.org/10.1016/j.jenvman.2023.118352.
[8] F. Eftekharipour, M. Jamshidi, R. Ghamarpoor, Fabricating core-shell of silane modified nano ZnO; Effects on photocatalytic degradation of benzene in air using acrylic nanocomposite, Alex. Eng. J. 70 (2023) 273–288, https://doi.org/10.1016/j.aej.2023.02.047.
[9] N. Moradi, M. Jamshidi, R. Ghamarpoor, M.R. Moghbeli, Surface functionalization/silane modification of CeO2 nanoparticles and their influences on photocatalytic activity of acrylic films for methylene blue removal, Prog. Org. Coat. 183 (2023) 107787, https://doi.org/10.1016/j.porgcoat.2023.107787.
[10] M.B. Öztürkmen, Y. Öz, N. Dilsiz, Physical and mechanical properties of graphene and h-Boron nitride reinforced hybrid aerospace grade epoxy nanocomposites, J. Appl. Polym. Sci. 140 (2023) e54639, https://doi.org/10.1002/app.54639.
[11] S.G.K. Bhagavatula, S.K. Painkal, R. Nanoth, K. Murugasamy, J. Karingamanna, Synergistic behavior of dual filler system (n -Si_3N_4 /COOH-MWCNT) on the mechanical, tribological, curing, and corrosion characteristics of epoxy hybrid nanocomposites, J. Appl. Polym. Sci. 140 (2023), https://doi.org/10.1002/app.53778.
[12] A. Maurya, S. Sinha, P. Kumar, V. Singh, A. review, Impact of surface treatment of nanofillers for improvement in thermo mechanical properties of the epoxy based nanocomposites, Mater. Today Proc 78 (2023) 164–172, https://doi.org/10.1016/j.matpr.2023.01.178.
[13] M. Sharif, A. Heidari, A. Aghaeinejad, Effect of ZnO-GO Particles on the Photopolymerization and Photo-Cleaning of Epoxy Coating, J. Photopolym. Sci. Technol. 32 (2019) 27–31, https://doi.org/10.2494/photopolymer.32.27.
[14] M. Sharif, S. Tavakoli, Biodegradable chitosan-graphene oxide as an affective green filler for improving of properties in epoxy nanocomposites, Int. J. Biol. Macromol. 233 (2023) 123550, https://doi.org/10.1016/j.ijbiomac.2023.123550.
[15] K. Dass, S. Chauhan, B. Gaur, Study on the effects of nano-aluminum-oxide particulates on mechanical and tribological characteristics of chopped carbon fiber reinforced epoxy composites, Proc. Inst. Mech. Eng. Part J. Mater. Des. Appl. 231 (2017) 403–422, https://doi.org/10.1177/1464420715598798.
[16] E. Bazireh, M. Sharif, Polythiophene-coated multi-walled carbon nanotube-reinforced epoxy nanocomposites for enhanced mechanical, electrical and thermal properties, Polym. Bull. 77 (2020) 4537–4553.
[17] Y. Che, Z. Sun, R. Zhan, S. Wang, S. Zhou, J. Huang, Effects of graphene oxide sheets-zirconia spheres nanohybrids on mechanical, thermal and tribological

performances of epoxy composites, Ceram. Int. 44 (2018) 18067–18077, https://doi.org/10.1016/j.ceramint.2018.07.010.
[18] A.U. Kini, M. Shettar, M.C. Gowrishankar, S. Sharma, A technical review on epoxy-nanoclay nanocomposites: mechanical, hygrothermal and wear properties, Cogent Eng 10 (2023) 2257949, https://doi.org/10.1080/23311916.2023.2257949.
[19] M. Naeem, H.-C. Kuan, A. Michelmore, Q. Meng, A. Qiu, M. Aakyiir, D. Losic, S. Zhu, J. Ma, A new method for preparation of functionalized graphene and its epoxy nanocomposites, Compos. Part B Eng. 196 (2020) 108096, https://doi.org/10.1016/j.compositesb.2020.108096.
[20] A. Bifulco, D. Parida, K.A. Salmeia, S. Lehner, R. Stämpfli, H. Markus, G. Malucelli, F. Branda, S. Gaan, Improving flame retardancy of in-situ silica-epoxy nanocomposites cured with aliphatic hardener: combined effect of DOPO-based flame-retardant and melamine, Compos. Part C Open Access 2 (2020) 100022, https://doi.org/10.1016/j.jcomc.2020.100022.
[21] P.Sarath Kumar, K. Jayanarayanan, B.D.S. Deeraj, K. Joseph, M. Balachandran, Synergistic effect of carbon fabric and multiwalled carbon nanotubes on the fracture, wear and dynamic load response of epoxy-based multiscale composites, Polym. Bull. 79 (2022) 5063–5084, https://doi.org/10.1007/s00289-021-03742-6.
[22] P.Sarath Kumar, K. Jayanarayanan, M. Balachandran, Thermal and Mechanical Behavior of Functionalized MWCNT Reinforced Epoxy Carbon Fabric Composites, Mater. Today Proc. 24 (2020) 1157–1166. https://doi.org/10.1016/j.matpr.2020.04.429.
[23] V.Y. Ignatenko, S.O. Ilyin, A.V. Kostyuk, G.N. Bondarenko, S.V. Antonov, Acceleration of epoxy resin curing by using a combination of aliphatic and aromatic amines, Polym. Bull. 77 (2020) 1519–1540, https://doi.org/10.1007/s00289-019-02815-x.
[24] J. Tian, X. Qi, C. Li, G. Xian, Friction behaviors and wear mechanisms of multi-filler reinforced epoxy composites under dry and wet conditions: effects of loads, sliding speeds, temperatures, water lubrication, Tribol. Int. 179 (2023) 108148, https://doi.org/10.1016/j.triboint.2022.108148.
[25] B. Wetzel, F. Haupert, M.Qiu Zhang, Epoxy nanocomposites with high mechanical and tribological performance, Compos. Sci. Technol. 63 (2003) 2055–2067, https://doi.org/10.1016/S0266-3538(03)00115-5.
[26] J. Yang, Z. Li, X. Feng, S. Nie, Construction of a binary architecture of flower-like nickel phyllosilicate@zinc sulfide towards the robust, wear-resistant and thermal-stable epoxy nanocomposites, Polym. Degrad. Stab. 207 (2023) 110224, https://doi.org/10.1016/j.polymdegradstab.2022.110224.
[27] A. Namdev, R. Purohit, A. Telang, A. Kumar, K.K. Saxena, S. Mabuwa, V. Msomi, K. A. Mohammed, Optimization of dry sliding wear behavior of epoxy nanocomposites under different conditions, Mater. Res. Express 9 (2022) 065303, https://doi.org/10.1088/2053-1591/ac7514.
[28] Md.Z. Hussain, S. Khan, P. Sarmah, Effect of dry sliding wear parameters on the specific wear rate of α-MnO_2 -epoxy nanocomposites, Proc. Inst. Mech. Eng. Part C J. Mech. Eng. Sci. 237 (2023) 1370–1392, https://doi.org/10.1177/09544062221132405.
[29] O.U. Colak, B. Birkan, O. Bakbak, A. Acar, D. Uzunsoy, Functionalized graphene-epoxy nanocomposites: experimental investigation of viscoelastic and viscoplastic behaviors, Mech. Time-Depend. Mater. 27 (2023) 185–205, https://doi.org/10.1007/s11043-021-09530-z.
[30] S.A. Al-Shawi, L.S. Alansari, A.A. Diwan, A. Alkhatat, Enhancement tensile strength, creep resistance and hardness of an epoxy resin by adding SiO_2 nanoparticles, IOP Conf. Ser. Mater. Sci. Eng. 1094 (2021) 012142, https://doi.org/10.1088/1757-899X/1094/1/012142.
[31] A. Khabaz-Aghdam, B. Behjat, L.F.M. Da Silva, E.A.S. Marques, A new theoretical creep model of an epoxy-graphene composite based on experimental investigation: effect of graphene content, J. Compos. Mater. 54 (2020) 2461–2472, https://doi.org/10.1177/0021998319895806.
[32] W. Jian, D. Lau, Creep performance of CNT-based nanocomposites: a parametric study, Carbon N Y 153 (2019) 745–756, https://doi.org/10.1016/j.carbon.2019.07.069.
[33] O. Starkova, S.T. Buschhorn, E. Mannov, K. Schulte, A. Aniskevich, Creep and recovery of epoxy/MWCNT nanocomposites, Compos. Part Appl. Sci. Manuf. 43 (2012) 1212–1218, https://doi.org/10.1016/j.compositesa.2012.03.015.
[34] A. Anand, P. Banerjee, D. Sahoo, D.K. Rathore, R.K. Prusty, B.C. Ray, Effects of temperature and load on the creep performance of CNT reinforced laminated glass fiber/epoxy composites, Int. J. Mech. Sci. 150 (2019) 539–547, https://doi.org/10.1016/j.ijmecsci.2018.09.048.
[35] W. Zhang, A. Joshi, Z. Wang, R.S. Kane, N. Koratkar, Creep mitigation in composites using carbon nanotube additives, Nanotechnology 18 (2007) 185703, https://doi.org/10.1088/0957-4484/18/18/185703.
[36] D.K. Rathore, R.K. Prusty, B.C. Ray, Mechanical, thermomechanical, and creep performance of CNT embedded epoxy at elevated temperatures: an emphasis on the role of carboxyl functionalization, J. Appl. Polym. Sci. 134 (2017), https://doi.org/10.1002/app.44851 app.44851.
[37] M. Rajabi, G.R. Rashed, D. Zaarei, Assessment of graphene oxide/epoxy nanocomposite as corrosion resistance coating on carbon steel, Corros. Eng. Sci. Technol. 50 (2015) 509–516, https://doi.org/10.1179/1743278214Y.0000000232.
[38] M. Bahrani, M. Sharif, K. Amirazodi, Preparation and characterization of polythiophene/graphene oxide/epoxy nanocomposite coatings with advanced properties, Polym. Bull. 79 (2022) 263–284, https://doi.org/10.1007/s00289-020-03529-1.
[39] M. Samardžija, V. Alar, V. Špada, I. Stojanović, Corrosion behaviour of an epoxy resin reinforced with aluminium nanoparticles, Coatings 12 (2022) 1500, https://doi.org/10.3390/coatings12101500.
[40] D.-W. Zhang, L. Chia, Y. Huang, Effect of carboxymethyl cellulose (CMC) functionalization on dispersion, mechanical, and corrosion properties of CNT/Epoxy nanocomposites, Chin. J. Polym. Sci. 41 (2023) 1277–1286, https://doi.org/10.1007/s10118-023-2928-0.
[41] A.A. Khan, A. Khan, Z. Zafar, I. Ahmad, Investigating the effect of curing temperature on the corrosion resistance of epoxy-based composite coatings for aluminium alloy 7075 in artificial seawater, RSC Adv 13 (2023) 21008–21020, https://doi.org/10.1039/D3RA04138G.
[42] A. Khan, M. Puttegowda, P. Jagadeesh, H.M. Marwani, A.M. Asiri, A. Manikandan, A.A. Parwaz Khan, G.M. Ashraf, S.M. Rangappa, S. Siengchin, Review on nitride compounds and its polymer composites: a multifunctional material, J. Mater. Res. Technol. 18 (2022) 2175–2193, https://doi.org/10.1016/j.jmrt.2022.03.032.
[43] N. Ramdani, J. Wang, H. Wang, T. Feng, M. Derradji, W. Liu, Mechanical and thermal properties of silicon nitride reinforced polybenzoxazine nanocomposites, Compos. Sci. Technol. 105 (2014) 73–79, https://doi.org/10.1016/j.compscitech.2014.10.006.
[44] W. Hao, W. Yang, H. Cai, Y. Huang, Non-isothermal crystallization kinetics of polypropylene/silicon nitride nanocomposites, Polym. Test. 29 (2010) 527–533, https://doi.org/10.1016/j.polymertesting.2010.03.004.
[45] Y. Zhang, M. Zhao, J. Zhang, Q. Shao, J. Li, H. Li, B. Lin, M. Yu, S. Chen, Z. Guo, Excellent corrosion protection performance of epoxy composite coatings filled with silane functionalized silicon nitride, J. Polym. Res. 25 (2018) 130, https://doi.org/10.1007/s10965-018-1518-2.
[46] J.L. Gómez-Magallón, J.A. Menchaca-Rivera, J. Pineda-Piñón, L.Ma. Avilés-Arellano, A. García-García, J.F.P. Robles, Improvement of the anticorrosive and thermal properties of an Epoxy-SiO2 coating due to the presence of silicon nitride, Prog. Org. Coat. 147 (2020) 105735, https://doi.org/10.1016/j.porgcoat.2020.105735.
[47] B. Yang, B. Chen, W. Dong, Y. Tong, J. Li, Nanohybrid of h-BN nanosheets supporting CeO_2 enhanced epoxy composite coatings with excellent self-lubricating performance, Polym. Compos. 44 (2023) 6440–6453, https://doi.org/10.1002/pc.27569.
[48] X. Liu, H. Liu, Y. Li, F. Teng, C. Liang, Superhydrophobic surface of hybrid nanocomposites made of TiO2 and multi-walled carbon nanotubes: photothermal ice removal performance and wear resistance, Appl. Surf. Sci. 640 (2023) 158318, https://doi.org/10.1016/j.apsusc.2023.158318.
[49] S. Mahaki, H. Khosravi, E. Tohidlou, Reinforcing effect of Fe_2O_3 nanoparticle-decorated graphene oxide on flexural and wear behaviors of epoxy composites, J. Appl. Polym. Sci. 139 (2022) e53228, https://doi.org/10.1002/app.53228.
[50] P.Bharti Shubham, R.K. Prusty, B.C. Ray, Tribological, mechanical, and thermal behavior of titanium dioxide and graphene nanoplatelet embedded epoxy based hybrid nanocomposite, Polym. Sci. Ser. A 64 (2022) 504–518, https://doi.org/10.1134/S0965545X22700328.
[51] B. Gopal Krishna, L. Snaha, N. Rasana, K. Jayanarayanan, Effect of nano silicon nitride integration on the curing performance of DGEBA epoxy matrix at ambient temperature, Mater. Lett. (2024) 137410, https://doi.org/10.1016/j.matlet.2024.137410.
[52] H. Wei, J. Xia, W. Zhou, L. Zhou, G. Hussain, Q. Li, K.(Ken) Ostrikov, Adhesion and cohesion of epoxy-based industrial composite coatings, Compos. Part B Eng. 193 (2020) 108035, https://doi.org/10.1016/j.compositesb.2020.108035.
[53] H. Xia, J. Li, K. Wang, X. Hou, T. Yang, J. Hu, Z. Shi, Superior wear resistance of epoxy composite with highly dispersed graphene spheres, Adv. Compos. Hybrid Mater. 5 (2022) 173–183, https://doi.org/10.1007/s42114-021-00259-4.
[54] P. Serles, H. Sun, G. Colas, J. Tam, E. Nicholson, G. Wang, J. Howe, A. Saulot, C. V. Singh, T. Filleter, Structure-dependent wear and shear mechanics of nanostructured MoS_2 coatings, Adv. Mater. Interfaces 7 (2020) 1901870, https://doi.org/10.1002/admi.201901870.
[55] N.L. Clelland, M.P. Pagnotto, R.E. Kerby, R.R. Seghi, Relative wear of flowable and highly filled composite, J. Prosthet. Dent. 93 (2) (2005) 153–157, https://doi.org/10.1016/j.prosdent.2004.11.006.
[56] J.F. Archard, Contact and rubbing of flat surfaces, J. Appl. Phys. 24 (1953) 981–988, https://doi.org/10.1063/1.1721448.
[57] Q.J. Wang, Y.-W. Chung (Eds.), Encyclopedia of Tribology, Springer US, Boston, MA, 2013, https://doi.org/10.1007/978-0-387-92897-5. https://link.springer.com/referencework/10.1007/978-0-387-92897-5.
[58] P.K. Prajapati, P. Biswas, B.K. Singh, C.O. Bapanapalle, R. Ghosh, N. Mandal, Reinforcing potential of MWCNTs on mechanical and machining performance of hot-pressed ZTA-MgO ceramic cutting inserts, Diam. Relat. Mater. 138 (2023) 110202, https://doi.org/10.1016/j.diamond.2023.110202.
[59] M. Zalaznik, M. Kalin, S. Novak, Influence of the processing temperature on the tribological and mechanical properties of poly-ether-ether-ketone (PEEK) polymer, Tribol. Int. 94 (2016) 92–97, https://doi.org/10.1016/j.triboint.2015.08.016.
[60] K. Vyavhare, P.B. Aswath, Tribological properties of novel multi-walled carbon nanotubes and phosphorus containing ionic liquid hybrids in grease, Front. Mech. Eng. 5 (2019) 15, https://doi.org/10.3389/fmech.2019.00015.
[61] Y.K. Wang, Z.W. Xu, L. Chen, Effect of carbon nanotubes on friction and wear properties of glass fiber/epoxy composites, Appl. Mech. Mater. 44-47 (2010) 2181–2185, https://doi.org/10.4028/www.scientific.net/AMM.44-47.2181.
[62] Y.-W. Mai, Z.-Z. Yu (Eds.), Polymer Nanocomposites, Woodhead Publ, Cambridge, England, 2006. ISBN-13: 978-1-85573-969-7, https://www.sciencedirect.com/book/9781855739697/polymer-nanocomposites.
[63] A.P. Kotula, J.W. Woodcock, J.W. Gilman, G.A. Holmes, A cure kinetics investigation of amine-cured epoxy by Rheo-Raman spectroscopy, Polymer (Guildf) 278 (2023) 125967, https://doi.org/10.1016/j.polymer.2023.125967.
[64] F.J. Cadete Santos Aires, J.C. Bertolini, On the use of silicon nitride in catalysis, Top. Catal. 52 (2009) 1492–1505, https://doi.org/10.1007/s11244-009-9296-z.

[65] M. Mohamed, M. Johnson, F. Taheri, On the thermal fatigue of a room-cured neat epoxy and its composite, Open J. Compos. Mater. 09 (2019) 145–163, https://doi.org/10.4236/ojcm.2019.92007.
[66] B. Kolesov, Hydrogen bonds: raman spectroscopic study, Int. J. Mol. Sci. 22 (2021) 5380, https://doi.org/10.3390/ijms22105380.
[67] H.-C. Tsai, F. Maryani, C.-C. Huang, T. Imae, J.-Y. Lin, Drug-loading capacity and nuclear targeting of multiwalled carbon nanotubes grafted with anionic amphiphilic copolymers, Int. J. Nanomedicine 4427 (2013), https://doi.org/10.2147/IJN.S53636.
[68] M. Remanan, M. Kannan, R.S. Rao, S. Bhowmik, L. Varshney, M. Abraham, K. Jayanarayanan, Microstructure development, wear characteristics and kinetics of thermal decomposition of hybrid nanocomposites based on poly aryl ether ketone, boron carbide and multi walled carbon nanotubes, J. Inorg. Organomet. Polym. Mater. 27 (2017) 1649–1663, https://doi.org/10.1007/s10904-017-0626-5.
[69] F. Valentini, A. Dorigato, A. Pegoretti, M. Tomasi, G.D. Sorarù, M. Biesuz, Si3N4 nanofelts/paraffin composites as novel thermal energy storage architecture, J. Mater. Sci. 56 (2021) 1537–1550, https://doi.org/10.1007/s10853-020-05247-5.
[70] A. Zambotti, E. Caldesi, M. Pellizzari, F. Valentini, A. Pegoretti, A. Dorigato, G. Speranza, K. Chen, M. Bortolotti, G.D. Sorarù, M. Biesuz, Polymer-derived silicon nitride aerogels as shape stabilizers for low and high-temperature thermal energy storage, J. Eur. Ceram. Soc. 41 (2021) 5484–5494, https://doi.org/10.1016/j.jeurceramsoc.2021.04.056.
[71] S. Rehman, S. Akram, A. Kanellopoulos, A. Elmarakbi, P.G. Karagiannidis, Development of new graphene/epoxy nanocomposites and study of cure kinetics, thermal and mechanical properties, Thermochim. Acta 694 (2020) 178785, https://doi.org/10.1016/j.tca.2020.178785.
[72] B.S. Mustafa, G.M. Jamal, O.Gh. Abdullah, The impact of multi-walled carbon nanotubes on the thermal stability and tensile properties of epoxy resin hybrid nanocomposites, Results Phys 43 (2022) 106061, https://doi.org/10.1016/j.rinp.2022.106061.
[73] J. Tang, K.X. Chen, C.S. Fu, Preparation and properties of β-Si3N4/epoxy matrix composite, Key Eng. Mater. 336 (2007) 1350–1352.
[74] S. Leena, R. Nanoth, J. Karingamanna, S.N. B, S.G.K. Bhagavatula, K.P. Rajan, A. Gopanna, Investigations on morphology, tribology, rheology, thermo-mechanical properties, and EMI shielding of WC/MWCNT nanohybrids in polypropylene, J. Reinf. Plast. Compos. (2024) 07316844241240565, https://doi.org/10.1177/07316844241240565.
[75] R. Bobbili, V. Madhu, Sliding wear behavior of E-glass-epoxy/MWCNT composites: an experimental assessment, Eng. Sci. Technol. Int. J. 19 (2016) 8–14, https://doi.org/10.1016/j.jestch.2015.07.008.
[76] K. Jayanarayanan, S. Thomas, K. Joseph, Morphology, static and dynamic mechanical properties of in situ microfibrillar composites based on polypropylene/poly (ethylene terephthalate) blends, Compos. Part Appl. Sci. Manuf. 39 (2008) 164–175, https://doi.org/10.1016/j.compositesa.2007.11.008.
[77] H. Ma, M.A. Aravand, B.G. Falzon, Phase morphology and mechanical properties of polyetherimide modified epoxy resins: a comparative study, Polymer (Guildf) 179 (2019) 121640, https://doi.org/10.1016/j.polymer.2019.121640.
[78] A. Surendran, J. Pionteck, N. Kalarikkal, S. Thomas, Mechanical responses of epoxy/cloisite nanocomposites, Mater. Chem. Phys. 281 (2022) 125755, https://doi.org/10.1016/j.matchemphys.2022.125755.
[79] K. Jayanarayanan, S. Thomas, K. Joseph, Dynamic mechanical analysis of in situ microfibrillar composites based on PP and PET, Polym.-Plast. Technol. Eng. 48 (2009) 455–463, https://doi.org/10.1080/03602550902727874.
[80] M.A. Sattar, A. Patnaik, Role of interface structure and chain dynamics on the diverging glass transition behavior of SSBR-SiO $_2$ -PIL elastomers, ACS Omega 5 (2020) 21191–21202, https://doi.org/10.1021/acsomega.0c02929.
[81] B. Bilyeu, W. Brostow, K.P. Menard, Separation of gelation from vitrification in curing of a fiber-reinforced epoxy composite, Polym. Compos. 23 (2002) 1111–1119, https://doi.org/10.1002/pc.10505.
[82] K. Deshmukh, T. Kovářík, A. Muzaffar, M. Basheer Ahamed, S.K. Khadheer Pasha, Mechanical analysis of polymers, Polym. Sci. Innov. Appl., Elsevier (2020) 117–152, https://doi.org/10.1016/B978-0-12-816808-0.00004-4.
[83] F. Meng, L. Liu, Electrochemical evaluation technologies of organic coatings (Eds.), in: J. Andres Perez-Taborda, A.G. Avila Bernal (Eds.), Coat. Thin-Film Technol., IntechOpen, 2019, https://doi.org/10.5772/intechopen.79736.
[84] A. Trentin, A. Pakseresht, A. Duran, Y. Castro, D. Galusek, Electrochemical characterization of polymeric coatings for corrosion protection: a review of advances and perspectives, Polymers (Basel) 14 (2022) 2306, https://doi.org/10.3390/polym14122306.
[85] Y. Liu, H. Li, Z. Li, EIS investigation and structural characterization of different hot-dipped zinc-based coatings in 3.5% NaCl solution, Int. J. Electrochem. Sci. 8 (2013) 7753–7767, https://doi.org/10.1016/S1452-3981(23)12843-4.
[86] H. Herrera Hernández, A.M. Ruiz Reynoso, J.C. Trinidad González, C.O. González Morán, J.G. Miranda Hernández, A. Mandujano Ruiz, J. Morales Hernández, R. Orozco Cruz, Electrochemical impedance spectroscopy (EIS): a review study of basic aspects of the corrosion mechanism applied to steels, in: M. El-Azazy, M. Min, P. Annus (Eds.), Electrochem. Impedance Spectrosc, IntechOpen, 2020, https://doi.org/10.5772/intechopen.94470.
[87] T.D. Mekuria, L. Wang, C. Zhang, M. Yang, Q. Lv, D.E. Fouad, Synthesis and characterization of high strength polyimide/silicon nitride nanocomposites with enhanced thermal and hydrophobic properties, Chin. J. Chem. Eng. 32 (2021) 446–453, https://doi.org/10.1016/j.cjche.2020.09.066.
[88] J.X.J. Zhang, K. Hoshino, Fundamentals of nano/microfabrication and scale effect, Mol.Sens. Nanodevices (2019) 43–111, https://doi.org/10.1016/B978-0-12-814862-4.00002-8.
[89] L. Qiu, D.A. Guzonas, J. Qian, Corrosion of silicon nitride in high temperature alkaline solutions, J. Nucl. Mater. 476 (2016) 293–301, https://doi.org/10.1016/j.jnucmat.2016.04.056.
[90] R.G. Munro, S.J. Dapkunas, Corrosion characteristics of silicon carbide and silicon nitride, J. Res. Natl. Inst. Stand. Technol. 98 (1993) 607, https://doi.org/10.6028/jres.098.040.
[91] M. Samardžija, I. Stojanović, M. Vuković Domanovac, V. Alar, Epoxy coating modification with metal nanoparticles to improve the anticorrosion, migration, and antibacterial properties, Coatings 13 (2023) 1201. https://doi.org/10.3390/coatings13071201.
[92] P.A. Schweitzer, Fundamentals of corrosion: mechanisms, causes, and Preventative Methods, CRC Press/Taylor & Francis, Boca Raton, Fla, 2010, https://doi.org/10.1201/9781420067712. https://www.taylorfrancis.com/books/mono/10.1201/9781420067712/fundamentals-corrosion-philip-schweitzer.
[93] H.H. Jasim, Evaluations of potable water tanks epoxy coatings performance using electrochemical impedance spectroscopic method, Al-Khwarizmi Eng. J (2017) 13, https://doi.org/10.22153/kej.2017.12.005.
[94] S. Masoumi, A.R. Miroliaei, Y. Jafarzadeh, Preparation and characterization of MWCNT-COOH/PVC ultrafiltration membranes to use in water treatment, (2018).
[95] L. Zhang, S. Bi, M. Liu, Lightweight electromagnetic interference shielding materials and their mechanisms, in: M.-G. Han (Ed.), Electromagn. Mater. Devices, IntechOpen, 2020. https://doi.org/10.5772/intechopen.82270.
[96] I.W. Nam, H.K. Lee, J.H. Jang, Electromagnetic interference shielding/absorbing characteristics of CNT-embedded epoxy composites, Compos. Part Appl. Sci. Manuf. 42 (2011) 1110–1118, https://doi.org/10.1016/j.compositesa.2011.04.016.
[97] M.A. Jusoh, K.Y. You, R. Nazlan, F. Esa, Electromagnetic shielding effectiveness of gypsum-magnetite composite at X-band frequency, Prog. Electromagn. Res. Lett 86 (2019) 21–26, https://doi.org/10.2528/PIERL19051401.